DEVELOPMENT OF PHOTOCATALYTIC MATERIALS FOR WATER OXIDATION AND CARBON DIOXIDE REDUCTION

by

Seif Momen Yusuf

A thesis submitted to the Faculty of the University of Delaware in partial fulfillment of the requirements for the degree of Master of Chemical Engineering

Fall 2012

© 2012 Seif Momen Yusuf
All Rights Reserved

DEVELOPMENT OF PHOTOCATALYTIC MATERIALS FOR WATER OXIDATION AND CARBON DIOXIDE REDUCTION

by

Seif Momen Yusuf

Approved: _____
Feng Jiao, Ph.D.
Professor in charge of thesis on behalf of the Advisory Committee

Approved: _____
Abraham M. Lenhoff, Ph.D.
Chair of the Department of Chemical and Biomolecular Engineering

Approved: _____
Babatunde A. Ogunnaike, Ph.D.
Interim Dean of the College of Engineering

Approved: _____
Charles G. Riordan, Ph.D.
Vice Provost for Graduate and Professional Education

TABLE OF CONTENTS

LIST OF TABLES v
LIST OF FIGURES vi
ABSTRACT viii

Chapter

1 INTRODUCTION 1

1.1 Motivation and Background 1
1.2 Research Objective 4
1.3 Experimental Information 5
1.4 Thesis Outline 6
1.5 References 8

2 NANOSTRUCTURED ALKALINE-CONTAINING δ-MANGANESE OXIDE FOR PHOTOCATALYTIC WATER OXIDATION 10

2.1 Introduction 10
2.2 Experimental Section 12

2.2.1 Synthesis of K-δ-MnO_2 nanosheets 12
2.2.2 Synthesis of K-δ-MnO_2 nanoparticles 12
2.2.3 Synthesis of Na-δ-MnO_2 nanosheets 12
2.2.4 Nanostructured H-δ-MnO_2 by proton ion exchange 12
2.2.5 Structural Characterization 13
2.2.6 Photocatalytic oxygen evolution from water 13

2.3 Results and Discussion 14
2.4 Conclusions 29
2.5 References 30

3 EFFECT OF THE SUPPORT ON THE PHOTOCATALYTIC WATER OXIDATION ACTIVITY OF COBALT OXIDE NANOCLUSTERS 31

3.1 Introduction 31
3.2 Experimental Methods 32

3.2.1 Synthesis of mesoporous silica KIT-6 32

3.2.2 Synthesis of mesoporous silica SBA-15 33
3.2.3 Synthesis of mesoporous silica supported Co_3O_4 catalysts 33
3.2.4 Synthesis of nanoparticle supported Co_3O_4 catalysts 34
3.2.5 Structural Characterization 34
3.2.6 Photocatalytic oxygen evolution from water 35

3.3 Results and Discussion 35
3.4 Conclusion 50
3.5 References 52

4 CONCLUSIONS AND PRELIMINARY WORK ON CARBON DIOXIDE REDUCTION CATALYSTS 53

4.1 Conclusions 53
4.2 Preliminary Work of Carbon Dioxide Reduction Catalysts 54

4.2.1 Introduction 54
4.2.2 Synthesis of supported Cu_xO_y catalysts 56
4.2.3 Structural Characterization 57
4.2.4 Results and Discussion 57

4.3 Future Work 63
4.4 References 64

LIST OF TABLES

Table 2.1: Oxygen production TOFs and BET surface areas of various δ-MnO_2 materials. 23

Table 2.2: Oxygen production TOFs and BET surface areas of various δ-MnO_2 materials 29

Table 3.1: Average cluster sizes estimated from TEM data and crystallinity sizes calculated from the Scherrer formula for all catalysts 39

Table 3.2: TOF's for all supported catalysts. 75mg of catalyst and 50mg of $Ru^{2+}(bpy)_3$ used for all measurements..... 43

Table 3.3: Photocatalytic oxygen evolution results for nanoparticle supports..... 50

LIST OF FIGURES

Figure 1.1: Schematic of photocatalyst system with a semiconductor as a light sensitizer and two catalysts 3

Figure 1.2: Diagram of steps in the $Ru^{2+}(bpy)_3$-$S_2O_8^{2-}$ system 6

Figure 2.1: Structure of (a) α-MnO_2, (b) β-MnO_2, (c)δ-MnO_2. Manganese atoms are blue and potassium ions are red..... 11

Figure 2.2: SEM images for as prepared nanostructured δ-MnO_2 materials (a) K-δ-MnO_2 nanosheets, (b) K-δ-MnO_2 nanoparticles, (c) K-δ-MnO_2 micron particles, (d) color-coded elemental mapping of K-δ-MnO_2 nanosheets (red color for K and blue color for Mn); SEM images for nanostructured δ-MnO_2 materials after proton ion exchanged, (e) H-δ-MnO_2 nanosheets and (f) H-δ-MnO_2 nanoparticles 15

Figure 2.3: HRTEM images for as-prepared (a) K-δ-MnO_2 nanosheets, (b) K-δ-MnO_2 nanoparticles, (c) H-δ-MnO_2 nanosheets and (d) H-δ-MnO_2 nanoparticles..... 17

Figure 2.4: PXRD patterns for (a) K-δ-MnO_2 nanosheets, (b) K-δ-MnO_2 nanoparticles, (c) K-δ-MnO_2 micron-sized particles, (d) H-δ-MnO_2 nanosheets, and (e) H-δ-MnO_2 nanoparticles..... 18

Figure 2.5: XANES data for (a) nanostructured and micron-sized K-δ-MnO_2 and (b) nanostructured H-δ-MnO_2 20

Figure 2.6: EXAFS data for all the δ-MnO_2 materials; curves are shifted along y-axis for display purpose..... 21

Figure 2.7: (a) SEM image, (b) HRTEM image, and (c) PXRD pattern for Na-δ-MnO_2 nanosheets..... 25

Figure 2.8: (a) XANES and (b) EXAFS results for K-δ-MnO_2 nanosheets and after photocatalytic water oxidation 27

Figure 3.1: TEM images for (a) KIT-6/Co_3O_4, (b) KIT-6/Co_3O_4-HEX, (c) KIT-6/Co_3O_4-PEN, and (d) SBA-15/Co_3O_4-HEX 37

Figure 3.2: (a) Low angle and (b) high angle PXRD patterns for KIT-6/Co_3O_4-WI, KIT-6/Co_3O_4-HEX, KIT-6/Co_3O_4-PEN, and SBA-15/Co_3O_4-HEX. A standard PXRD pattern for bulk Co_3O_4 is also shown in (b) for comparison 40

Figure 3.3 Sensitizer-TOF relationship using KIT-6/Co_3O_4-HEX as the catalysts 42

Figure 3.4: Low and high angle PXRD patterns for KIT-6/Co_3O_4-HEX before and after photocatalysis. 45

Figure 3.5: PXRD patterns for as-prepared Co_3O_4 nanoparticles, nano-SiO_2/Co_3O_4 and nano-Al_2O_3/Co_3O_4 47

Figure 3.6: TEM and HRTEM images for (top) as-made Co_3O_4 nanoparticles, (middle) nano-SiO_2/Co_3O_4, and (bottom) nano-Al_2O_3/Co_3O_4 49

Figure 4.1: PXRD patterns for Cu_xO_y/SBA-15 (10%wt/wt) catalysts. (a) 10%wt/wt catalyst before H_2 reduction, (b) low angle plot of 10% wt/wt catalyst after H_2 reduction at 250°C, (c) wide angle plot of 10% wt/wt catalyst after H_2 reduction at 125°C, (d) wide angle plot of 10% wt/wt catalyst after H_2 reduction at 250°C and 150°C 58

Figure 4.2: TEM images of Cu_xO_y/SBA-15 catalyst reduced at 250°C: (a) 1.0% wt/wt, (b) 4.8% wt/wt, and (c) 10% wt/wt 59

Figure 4.3: In-situ GTIR system with photoreactor (left), Masterflex pump (middle) and Bruker ALPHA FTIR unit with flow through attachment (right) 61

Figure 4.4: Background IR spectra for carbon dioxide reduction system 62

ABSTRACT

Fossil fuels are currently the primary energy source of the world, but are an undesirable energy source for the future as their combustion generates CO_2, a greenhouse gas and it is unlikely current reserves of fossil fuel will meet future energy demand. One alternative is to use solar energy, which provides more than enough energy to meet demand, to produce carbonaceous fuels. These solar fuels are advantageous because their generation uses H_2O, which is abundant, and CO_2, which needs to be removed from the atmosphere. The oxidation of H_2O is needed to the electrons needed for the reduction of CO_2 In this thesis, nanostructured manganese and cobalt oxide catalysts were synthesized and systematically investigated as cheap, stable, and efficient H_2O oxidation catalysts.

The first part of research mainly focused on the development of highly efficient manganese based oxygen evolution catalysts and investigation of effects of alkaline cations in the photocatalytic water oxidation reaction. K^+ containing and Na^+ containing δ-MnO_2 catalysts were synthesized using a hydrothermal synthetic approach. To determine the effect of alkaline ions, K^+ in δ-MnO_2 was replaced by H^+ ions using an ion-exchange process. The K-δ-MnO_2 and Na-δ-MnO_2 catalysts had TOF's about one order of magnitude higher than their H-δ-MnO_2 counterparts, even though the H-δ-MnO_2 catalysts have much larger surface areas. The H-δ-MnO_2 may have had lower activity because the $Ru^{2+}(bpy)_3$ was too large to access the new surface sites. The results suggest that the alkaline cations stabilize the MnO_2 layers and are not directly involved in the H_2O oxidation reaction.

Turning to cobalt based oxygen evolution catalysts, it has been shown in previous reports that Co_3O_4 supported in mesoporous silica exhibited high oxygen evolution activities, while there is still no report on systematic study of support effect. In this thesis, Co_3O_4 nanoclusters supported in various materials were studied. Wet-impregnation and bi-solvent methods were used to fabricate mesoporous silica with Co_3O_4 clusters. Hexane/water was found to be the optimal combination yielding a catalyst with a small particle size and narrow size distribution. The results confirmed that as the Co_3O_4 cluster size became smaller, the water oxidation activity increased. KIT-6 was found to be a better support than SBA-15, due to its 3D porous structure offering a more accessible system. Bare Co_3O_4 nanoparticles and particles supported by SiO_2 and Al_2O_3 were also studied so that the role of support could be determined. It was found that the supported particles had higher activity than the bare particle, but there were no significant differences in activity between the two supported particles. This indicates that the surface is not directly involved in the reaction and the key role of the support in photocatalytic water oxidation reaction is to physically separate and immobilize the Co_3O_4 nanoclusters.

Chapter 1

INTRODUCTION

1.1 Motivation and Background

One of the major challenges facing the world today is finding a clean and renewable energy source. Global energy demand is expected to more than double by 2050 (from 13 to 28-35 TW/year)[1], fossil fuels, the current primary energy source, will likely be unable to meet future energy demands. Even though fossil fuels are currently the most convenient energy source available and there is still a large amount that has not been extracted, fossil fuels are still not desirable sources of energy for the future because the burning of fossil fuels generates CO_2, which is a greenhouse gas. Levels of CO_2 in the atmosphere have been steadily increasing over the past few decades due to the increase in energy demand. Studies on the atmospheric CO_2 concentration have been correlated with temperature swings that have caused ice ages on the planet[2]. Various climate models predict that increased amounts of atmospheric CO_2 could cause changes in the water cycle or a significant increase in sea level. Since there is no natural process for the consumption of CO_2, it will stay in the atmosphere for long periods of time unless it is consumed in another process. In order to avoid any of these long term issues, an alternative energy source must be utilized to meet energy demand so that the dependence on fossil fuels can decrease.

The sun is a clean, renewable energy source that deposits 120,000 TW of radiation to the earth each year, which is more than enough to meet growing energy demand. Unlike fossil fuels the distribution of sunlight is not affected by politics and

there are some of the areas in the world that are almost constantly bathed in sunlight, such as the Sahara and Gobi deserts[3], so the amount of sunlight is large enough that there will be more than enough energy available to meet energy demand. In order to be utilized effectively, solar energy must be captured and converted into another form that can be easily stored. Plants accomplish this through the process of photosynthesis, using solar energy to reduce carbon dioxide into sugars, which are then used as chemical energy sources to help plants grow. This process can be mimicked artificially through photocatalysis, the utilization of absorbed solar energy to generate excited electrons and holes that can be used to drive a chemical reaction with the help of a catalyst particle.

Specifically, photocatalysis can be used to reduce CO_2 to CH_3OH, which can serve as liquid fuel. In order to complete CO_2 reduction, there needs to be a reaction that generates the necessary electrons and H^+ ions. In nature, plants oxidize H_2O as the source of the necessary electrons for the conversion of CO_2 to sugars. H_2O is the only cheap and abundant source that is able to supply H^+ ions and electrons on a terawatt scale[4-14]. This makes the oxidation of H_2O a critical reaction because without the electrons and H^+ ions that this reaction produces, it will be impossible to generate any solar fuel, such as H_2 and CH_3OH. It is critical to develop catalysts that can effectively promote H_2O oxidation as well as a system to couple this reaction with CO_2 reduction.

The original work that inspired the field of photocatalysis was done in 1972 by Fujishima and Honda[15]; a photoelectrochemical cell (PEC) was constructed with a TiO_2 anode and a Pt cathode. The TiO_2 anode was irradiated with ultraviolet light, exciting electrons and generating holes; the electrons and holes were then used to split

H_2O into O_2 and H_2. It was found that the holes oxidized H_2O into O_2 at the TiO_2 anode while the electrons produced H_2 at the Pt cathode. The Pt acted as a co-catalyst to the TiO_2, helping to separate the excited electrons from the holes and subsequently increasing the rate of H_2 production.

A few issues with this photocatalyst system prevent it from becoming competitive with fossil fuels on a large scale: TiO_2 is only capable of utilizing ultraviolet light and Pt is prohibitively expensive. An alternate system for solar fuel production through photocatalysis, consists of a semiconductor particle and two catalysts, one that promotes oxidation reactions and another that promotes reduction reactions (Figure 1.1).

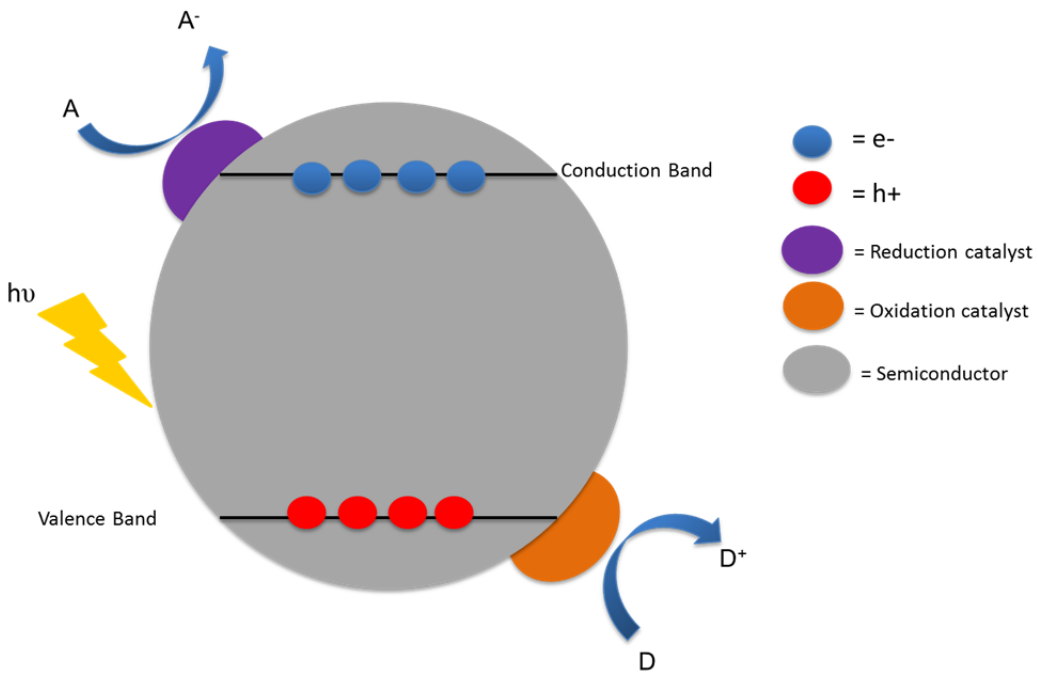

Figure 1.1: Schematic of photocatalyst system with a semiconductor as a light sensitizer and two catalysts

The semiconductor acts as the light sensitizer, absorbing the light and separating the excited electrons and holes. The electrons and holes can then migrate towards the reduction and oxidation catalysts, respectively. The catalysts then serve as sites for electron or hole transfer to the species that were adsorbed on the catalyst in order drive a chemical reaction. This system is more flexible than the PEC system because each component only has to fulfill one role. The semiconductor only has to be able to absorb visible light and be able to separate electrons and holes and each catalyst has to act of a site for holes or electrons so that they can be separated from each other and be easily transferred to any reactants. In order to produce solar fuels one catalyst will be designed for H2O oxidation (reaction 1) and the second catalyst will be designed for CO2 reduction (reaction 2).

$$H_2O \rightarrow O_2 + 4e^- + 4H^+ \qquad (1)$$

$$CO_2 + 6e^- + 6H^+ \rightarrow CH_3OH + H_2O \qquad (2)$$

Both of these reactions have to be coupled together in order to produce any solar fuels as H2O oxidation supplies to necessary electrons and hydrogen ions for CO2 reduction.

1.2 Research Objective

The primary objective of my research is the development of catalysts for H_2O oxidation. The proposed catalyst will have to be stable, able to promote its particular reaction with a high turnover frequency(TOF) and high selectivity, and composed of abundant and cheap materials in order to ensure economic viability. The catalysts

should not have to be able to effectively absorb light and separate electrons and holes; they have to be able to transfer holes to adsorbed water in order to evolve oxygen.

1.3 Experimental Information

In order to determine the activity of the catalysts for water oxidation, the previously mentioned semiconductor system cannot be used. This is because if the catalyst is combined with a seminconductor, the overall TOF will be affected by the semiconductor's ability to separate electrons and holes. In order to evaluate the activity of the catalyst without any other factors, a $Ru^{2+}(bpy)_3$(bpy=2,2' bipyridine) - $S_2O_8^{2-}$ system is used, which was designed to mimic water oxidation in plants. Plants are able to effectively use visible light to catalyze water oxidation through the combination of chrolophyll complexes, to absorb light and separate holes and electrons, and a $CaMn_4O_4$[16-18] complex, to act as the site of water oxidation. In $Ru^{2+}(bpy)_3$- $S_2O_8^{2-}$ system, $Ru^{2+}(bpy)_3$ absorbs visible light and generates electron-hole pairs. The photogenerated electrons are taken up by the sacrificial electron acceptor $S_2O_8^{2-}$, which causes $Ru^{2+}(bpy)_3$ to be oxidized to $Ru^{3+}(bpy)_3$ and $S_2O_8^{2-}$ to be reduced to a SO_4^{2-} molecule and $SO_4^{-}\cdot$ radical. The SO_4^{-} radical can subsequently oxidize another to $Ru^{2+}(bpy)_3$, which means one photon can generate two$Ru^{3+}(bpy)_3$ molecules. The $Ru^{3+}(bpy)_3$ then donates the photogenerated holes to catalyst, reducing the molecule back to $Ru^{2+}(bpy)_3$. Once this cycle is repeated twice, one O_2 molecule can be produced.

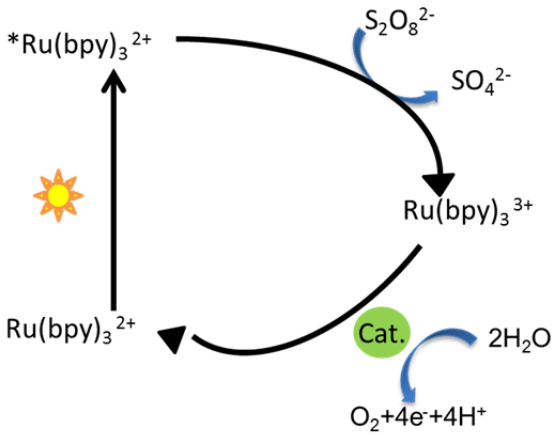

Figure 1.2: Diagram of steps in the $Ru^{2+}(bpy)_3$-$S_2O_8^{2-}$ system

Using $Ru^{2+}(bpy)_3$ (bpy=2,2'-bipyridine) as the sensitizer and sodium persulfate as the sacrificial electron acceptor, Mallouk and his co-workers demonstrated that IrO_2 colloid is a remarkable catalyst for water oxidation with a TOF of 40 s^{-1} per surface Ir atom under an aqueous environment (pH 5.7, 25°C)[7]. As alternatives, first row transition metal oxides, e.g. manganese and cobalt oxides, have attracted much attention as potential water oxidation catalysts, because they are abundant and cheap[19-28].

1.4 Thesis Outline

This thesis focuses on the synthesis, characterization, and photocatalytic testing of manganese and cobalt oxide H_2O oxidation catalysts. For manganese oxides, δ-phase MnO_2 was chosen. Recent work[23] with MnO_2 catalysts had shown that the crystal phase and morphology of α and β phase MnO_2 particles did not have a significant effect on H_2O oxidation activity and that the critical factor for determining H_2O oxidation activity was the surface area of the catalyst. However, it was found

that the α-phase contained K^+ ions while the β-phase did not and since K^+ ions could not easily be removed from the α-phase particles, the effect of the K^+ ions could not be studied with these phases. The δ-phase of MnO_2 has a layered crystal structure so it is easy to remove the K^+ ions and replace them with H^+ ions. Studies were also done of δ-phase MnO_2 catalysts that contained Na^+ instead of K^+ ions so that the effect of alkaline ions on MnO_2 water oxidation catalysts could be studied.

Co_3O_4 particles supported by mesoporous silica were chosen as the cobalt oxide water oxidation catalyst. The pores of mesoporous silica allow for the formation of stable nanoparticles without the use of surfactants. Previous work[20] had studied Co_3O_4 nanoclusters that were loaded onto SBA-15, a mesoporous silica, through the wet impregnation method. It was found that the 4wt% sample showed the highest activity, likely due to the smaller cluster size. It was also found that the supported Co_3O_4 clusters performed better than unsupported Co_3O_4 particles, implying that the support may assist the water oxidation process. In order to improve the supported Co_3O_4 water oxidation catalyst, new impregnation techniques were studied with two different mesoporous silicas, KIT-6 and SBA-15. These two supports were chosen because they have similar pore size distributions, but KIT-6 has 3D pores while SBA-15 has 1D pores. Additionally, the effect of the support was tested by comparing the activity of 6nm Co_3O_4 particles that are unsupported to those supported by SiO_2 and Al_2O_3 particles.

1.5 References

(1) Nocera, D. G. *Daedalus* **2006**, *135*, 112.

(2) Lewis, N. S.; Nocera, D. G. *Proceedings of the National Academy of Sciences of the United States of America* **2007**, *104*.

(3) McDaniel, N. D.; Bernhard, S. *Dalton Transactions* **2010**, *39*.

(4) Matsumoto, Y.; Sato, E. *Electrochimica Acta* **1979**, *24*.

(5) Okuno, Y.; Yonemitsu, O.; Chiba, Y. *Chemistry Letters* **1983**.

(6) Harriman, A.; Pickering, I. J.; Thomas, J. M.; Christensen, P. A. *Journal of the Chemical Society-Faraday Transactions I* **1988**, *84*, 2795.

(7) Hara, M.; Waraksa, C. C.; Lean, J. T.; Lewis, B. A.; Mallouk, T. E. *Journal of Physical Chemistry A* **2000**, *104*, 5275.

(8) Brimblecombe, R.; Swiegers, G. F.; Dismukes, G. C.; Spiccia, L. *Angewandte Chemie-International Edition* **2008**, *47*.

(9) Kanan, M. W.; Nocera, D. G. *Science* **2008**, *321*, 1072.

(10) Esswein, A. J.; McMurdo, M. J.; Ross, P. N.; Bell, A. T.; Tilley, T. D. *Journal of Physical Chemistry C* **2009**, *113*, 15068.

(11) Kohl, S. W.; Weiner, L.; Schwartsburd, L.; Konstantinovski, L.; Shimon, L. J. W.; Ben-David, Y.; Iron, M. A.; Milstein, D. *Science* **2009**, *324*.

(12) Lutterman, D. A.; Surendranath, Y.; Nocera, D. G. *Journal of the American Chemical Society* **2009**, *131*.

(13) Risch, M.; Khare, V.; Zaharieva, I.; Gerencser, L.; Chernev, P.; Dau, H. *Journal of the American Chemical Society* **2009**, *131*.

(14) Brimblecombe, R.; Koo, A.; Dismukes, G. C.; Swiegers, G. F.; Spiccia, L. *Chemsuschem* **2010**, *3*.

(15) Fujishima, A.; Honda, K. *Nature* **1972**, *238*, 37.

(16) Yano, J.; Kern, J.; Sauer, K.; Latimer, M. J.; Pushkar, Y.; Biesiadka, J.; Loll, B.; Saenger, W.; Messinger, J.; Zouni, A.; Yachandra, V. K. *Science* **2006**, *314*, 821.

(17) Barber, J. *Chemical Society Reviews* **2009**, *38*, 185.

(18) Umena, Y.; Kawakami, K.; Shen, J. R.; Kamiya, N. *Nature* **2011**, *473*, 55.

(19) Jiao, F.; Frei, H. *Chemical Communications* **2010**, *46*, 2920.

(20) Jiao, F.; Frei, H. *Angewandte Chemie-International Edition* **2009**, *48*, 1841.

(21) Najafpour, M. M.; Ehrenberg, T.; Wiechen, M.; Kurz, P. *Angewandte Chemie-International Edition* **2010**, *49*, 2233.

(22) Robinson, D. M.; Go, Y. B.; Greenblatt, M.; Dismukes, G. C. *Journal of the American Chemical Society* **2010**, *132*, 11467.

(23) Boppana, V. B. R.; Jiao, F. *Chemical Communications* **2011**, *47*, 8973.

(24) Shevchenko, D.; Anderlund, M. F.; Thapper, A.; Styring, S. *Energy & Environmental Science* **2011**, *4*.

(25) Man, I. C.; Su, H.-Y.; Calle-Vallejo, F.; Hansen, H. A.; Martinez, J. I.; Inoglu, N. G.; Kitchin, J.; Jaramillo, T. F.; Norskov, J. K.; Rossmeisl, J. *Chemcatchem* **2011**, *3*.

(26) McCool, N. S.; Robinson, D. M.; Sheats, J. E.; Dismukes, G. C. *Journal of the American Chemical Society* **2011**, *133*.

(27) Iyer, A.; Del-Pilar, J.; King'ondu, C. K.; Kissel, E.; Garces, H. F.; Huang, H.; El-Sawy, A. M.; Dutta, P. K.; Suib, S. L. *Journal of Physical Chemistry C* **2012**, *116*.

(28) Moonshiram, D.; Jurss, J. W.; Concepcion, J. J.; Zakharova, T.; Alperovich, I.; Meyer, T. J.; Pushkar, Y. *Journal of the American Chemical Society* **2012**, *134*.

Chapter 2

NANOSTRUCTURED ALKALINE-CONTAINING δ-MANGANESE OXIDE FOR PHOTOCATALYTIC WATER OXIDATION

2.1 Introduction

For example, we recently reported the utilization of manganese and cobalt oxides nanoclusters inside mesoporous supports for artificial water oxidation applications in visible light[1, 2]. The higher activity for these nano-catalysts compared with their micron sized counterparts was attributed in part to the high surface areas afforded by the small nanoclusters inside the pores of the silica supports. We then proceeded to systematically investigate the influence of crystal structure of manganese oxide systems on the water oxidation activity[3]. All the samples exhibited high TOFs and we concluded that the morphology and crystal structure have negligible effect on water oxidation activity for MnO_2 catalysts, while larger surface areas significantly enhanced their activity in line with our earlier studies with silica supports. We also noted in that work that the presence of potassium in α-MnO_2 nanotubes improves the activity and this report extends on this hypothesis by carefully elucidating the effect of potassium on the water oxidation activity by discounting other variables like surface area, crystal structure and morphology.

Manganese (IV) oxide exists in multiple polymorphs: α, β and δ-MnO_2. All of these four crystal structures are made of [MnO_6] octahedrals, α, and β MnO_2 are respectively based of 2×2, and 1×1, Mn octahedral tunnels whereas δ-MnO_2 has a layered structure (see Figure 2.1)[4]. Of these four major polymorphs of MnO_2, α-MnO_2

and δ-MnO_2 have channels big enough to uptake guest cations like K^+, which has been noted in earlier studies by Komaba et al. and our earlier work[3, 5]. The latter δ-MnO_2 polymorph forms the basis of this study, since its layers can incorporate a higher fraction of K^+. Due to this property, this material is known to favor the diffusion of Li^+ and has therefore already been investigated for lithium battery applications[4]. On the other hand, β-MnO_2 has the smallest channels formed by 1×1 edge-shared Mn octahedrals, and shows no capability in uptaking any guest cations. These variations in the uptake of cations (in our case, K^+ and Na^+) prompted us to systematically analyze the effect of alkaline cations on the water oxidation activity with manganese oxide systems as this has not been explored so far. This work proves that alkaline containing δ-MnO_2 materials are effective water oxidation catalysts.

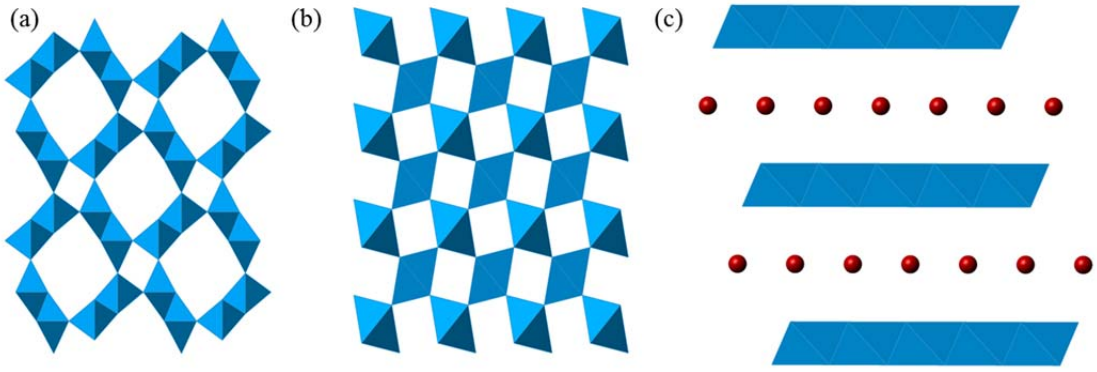

Figure 2.1: Structure of (a) α-MnO_2, (b) β-MnO_2, (c)δ-MnO_2. Manganese atoms are blue and potassium ions are red

2.2 Experimental Section

2.2.1 Synthesis of K-δ-MnO_2 nanosheets

This procedure is modified based on a reported approach[6]. In a typical synthesis of K-δ-MnO_2 nanosheets (with K), 0.948 g of $KMnO_4$ was dissolved in water, followed by addition of 0.169 g of $MnSO_4$ under stirring. The mixture was transferred and sealed in a hydrothermal bomb with PTFE liner, followed by a thermal treatment in an oven at 160^{o}C for 12 h. After cooling to room temperature, the resulting mixture was filtered, washed by water, and dried at 60^{o}C.

2.2.2 Synthesis of K-δ-MnO_2 nanoparticles

1 g of $KMnO_4$ was calcined at 300^{o}C under air for 3h to form the corresponding K-δ-MnO_2 phases. The resulting materials are dispersed in 200 mL of DI water and sonicated for 30 mins, followed by filtering and washing with water for several times. The final samples are dried under air at 60^{o}C.With a similar procedure, $KMnO_4$ was calcined at 800^{o}C to obtain micron-sized K-δ-MnO_2 particles[7].

2.2.3 Synthesis of Na-δ-MnO_2 nanosheets

In a typical synthesis of Na-δ-MnO_2 nanosheets (with Na), 100 mL $Mn(NO_3)_2$ aqueous solution (containing 3mmol of Mn) is slowly added into a mixture of 180 mL of NaOH aqueous solution (containing 6.88 g of NaOH) and 20 mL of 30% H_2O_2 under stirring. After stirring at room temperature for 1 h, the resulting precipitate is centrifuged and washed by water, and dried at 60^{o}C.[8]

2.2.4 Nanostructured H-δ-MnO_2 by proton ion exchange

1 g of as-synthesized K-δ-MnO_2 (nanosheets and nanoparticles) was dispersed in 100 mL of 0.7M HNO_3 aqueous solution. The mixture was heated to 60^{o}C for 90

mins before cooling to room temperature. The mixture was filtered, washed with water, and dried at 60^{o}C.

2.2.5 Structural Characterization

Scanning electron microscope (SEM) images were recorded on a JEOL JSM 7400F microscope with a field emission gun capable of 1.5 nm resolution. The imaging using the SEM and elemental analysis with mapping using energy dispersive analysis (EDX) was done at a voltage of 3 kV and 15 kV, respectively. Transmission electron microscope (TEM) images were recorded on a field emission transmission electron microscope JEM-2010F FasTEM. Powder X-ray diffraction (PXRD) results were collected on a Philips X'pert diffractometer using a Cu Kα source with a scan of 2 s/step and a step size of 0.02^{o} 2θ. Adsorption isotherms were collected on a Micromeritics ASAP 2010 at 77 K using N_2 as the adsorbent gas. Surface areas were evaluated using the BET theory from P/P_0 region of 0.05 to 0.4. All the samples were degassed at 423 K under vacuum before the measurements. X-ray absorption experiments were performed at beamline X10c at NSLS, through a user proposal (PASS form number 20026). The XAS data were processed using a free software Athena.

2.2.6 Photocatalytic oxygen evolution from water

Photochemical water oxidation experiments were conducted in a 100 mL reactor containing 40 mL of aqueous buffer (Na_2SiF_6-$NaHCO_3$, 0.022-0.028 M) with pH held at 5.8, 390 mg Na_2SO_4, 130 mg $Na_2S_2O_8$, 45 mg $[Ru(bpy)_3]Cl_2 \cdot 6H_2O$, and 100 mg Mn oxide catalyst. The reactor was irradiated with a 300W Xe research lamp (UV fused silica, 1.3in collimated, F/1, 1.5inch) with 400 nm cut-off filter. The

resulting O_2 molecules in the head space were quantitatively analyzed by a Shimadzu gas chromatography system (Shimadzu 2014). All the experiments are conducted at room temperature (~ 25 ^oC). A base-line is recorded for each test before exposure to Xe lamp.

2.3 Results and Discussion

Several techniques detailed in literature were employed to synthesize nanostructured K-δ-MnO_2. K-δ-MnO_2 nanosheets were synthesized according to the procedure reported by Li[6]. To clarify the effect of morphology, K-containing δ-MnO_2 nanoparticles were also synthesized through a solid state reaction of thermal decomposition of $KMnO_4$ at 300^oC[7]. A K-δ-MnO_2 material with a much larger particle size and lower surface area was synthesized by the same technique at a higher calcination temperature (800^oC) in order to facilitate the investigation of surface effects in photocatalytic water oxidation. Also, proton ion exchange was performed for both K-δ-MnO_2 nanosheets and nanoparticles to replace K^+ with H^+ in the δ-MnO_2 structures. All the synthesis conditions are detailed in the experimental section.

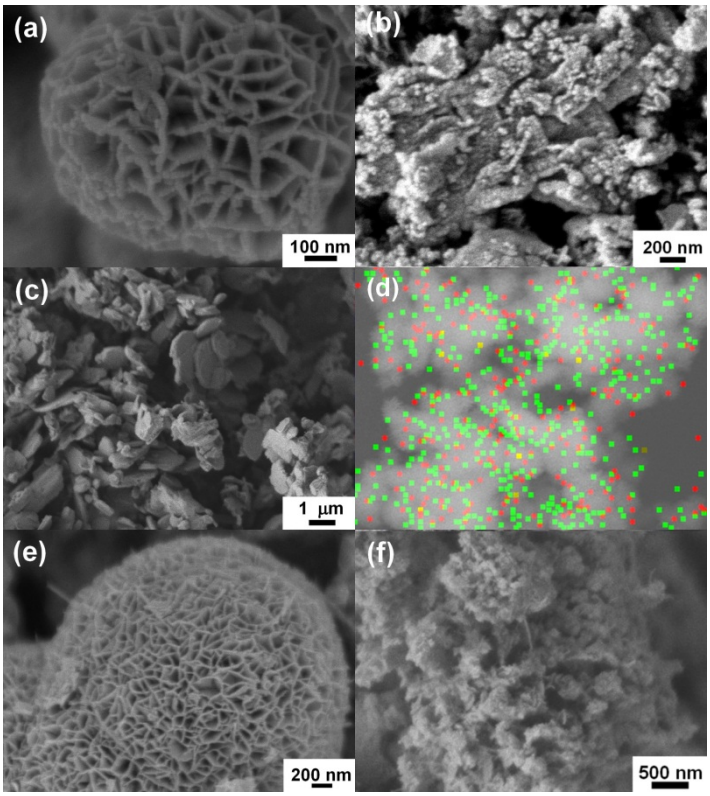

Figure 2.2: SEM images for as prepared nanostructured δ-MnO_2 materials (a) K-δ-MnO_2 nanosheets, (b) K-δ-MnO_2 nanoparticles, (c) K-δ-MnO_2 micron particles, (d) color-coded elemental mapping of K-δ-MnO_2 nanosheets (red color for K and blue color for Mn); SEM images for nanostructured δ-MnO_2 materials after proton ion exchanged, (e) H-δ-MnO_2 nanosheets and (f) H-δ-MnO_2 nanoparticles

We first examined the morphologies of K-δ-MnO_2 samples using scanning electron microscopy (SEM). The SEM image (Figure 2.2a) clearly show that the morphology of K-δ-MnO_2 prepared via hydrothermal reaction is of spheres comprised of nanosheets. These spheres are about 1 μm in diameter and its nanosheets are around 10-20 nm thick. In the cases of K-δ-MnO_2 prepared through thermal decomposition reaction at 300^{o}C and 800^{o}C, no such morphology is observed (Figures 2.2b and 2.2c). The 300^{o}C sample contains small particles with a dimension of 10-200 nm, while the

800°C sample has an average particle size of 0.5-1 μm. Energy-dispersive X-ray spectroscopy (EDX) measurements show that K-δ-MnO_2 nanosheets and K-δ-MnO_2 samples synthesized by solid state reaction have significant potassium contents with the K/Mn ratio between 0.30 to 0.34 (see Table 2.1). Color-coded SEM elemental mapping was then employed to verify the uniform distribution of potassium because the intensity and spread of the color is proportional to the corresponding element's concentration. These results presented in Figure 1d show that K is distributed uniformly with Mn in all the δ-MnO_2 particles (Figure 2.2d).

These results are in contrast to the potassium contents observed after proton ion exchange. Reaction of the K-δ-MnO_2 samples with 0.7M of HNO_3 reduces the K/Mn ratio from ~0.32 to 0.02. This suggests that K^+ cations in the layered δ-MnO_2 structure are leached away and replace with H^+ under aggressive acid treatment. The H-δ-MnO_2 nanosheets prepared through hydrothermal reaction maintain their morphology after acid treatment (Figure 2.2e), while K-δ-MnO_2 nanoparticles prepared at 300°C became rougher on the surface and some nanorod-like particles were observed after proton exchange (Figure 2.2f).

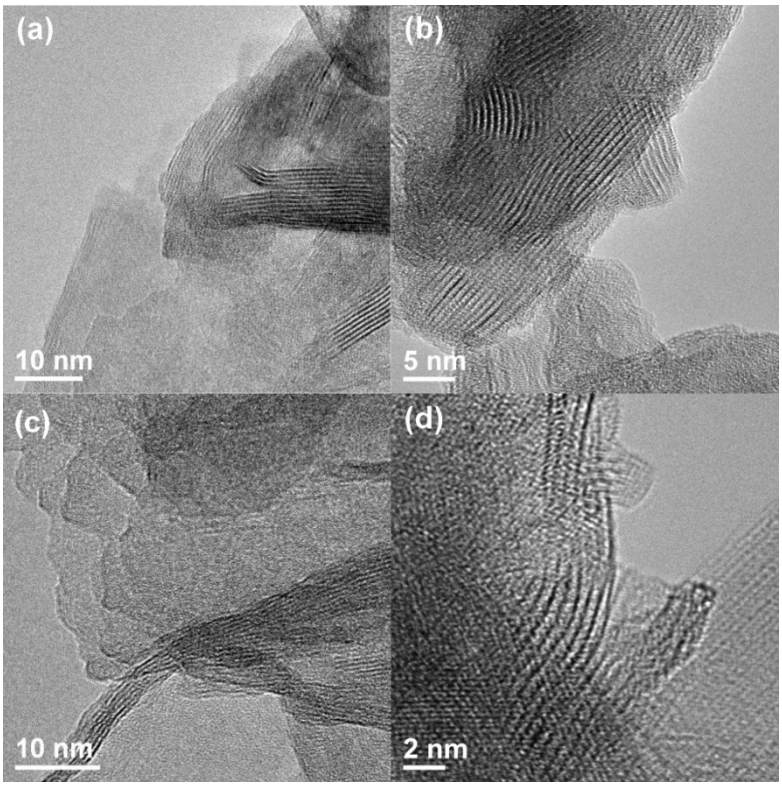

Figure 2.3: HRTEM images for as-prepared (a) K-δ-MnO_2 nanosheets, (b) K-δ-MnO_2 nanoparticles, (c) H-δ-MnO_2 nanosheets and (d) H-δ-MnO_2 nanoparticles

We performed high-resolution transmission electron microscopy (HRTEM) to further explore the structural details of K-δ-MnO_2 samples. The HRTEM images in Figure 2 show that both as-prepared K-δ-MnO_2 samples are composed of MnO_2 nanosheets with the same interlayer distance (~0.66 nm), indicating both materials have a similar crystal structure. This is further confirmed by powder X-ray diffraction (PXRD) analysis. The PXRD patterns (Figure 2.3) confirm the formation of the desired δ-MnO_2 polymorph as all the observed reflections were indexed to its well-known layered structure. The representative (00c) peaks are at ~12.4, 24.8 and 36.3^o (2θ).

The HRTEM images for samples after proton exchange (Figures 2.3c and 2.3d) clearly show that δ-MnO_2 layered feature in both materials are maintained, although in the case of H- δ-MnO_2 nanaoparticles some nanorod like H- δ-MnO_2 particles are also observed which is consistent with the SEM results. The preservation of δ-MnO_2 crystal structure was further investigated by PXRD analysis, shown in Figure 2.4. Note that the diffraction peaks from (00c) planes are still present. This indicates that the δ-MnO_2 structure is intact, although the relative intensities are slightly different. This could be due to partial destabilization of the layered structure from the leaching of K^+ cations. This destabilization also causes a significant increase in the surface area of δ-MnO_2 materials after proton exchange, for example the surface area of the nanosheets increases from 35.7 m^2/g to 151 m^2/g after the potassium is leached away.

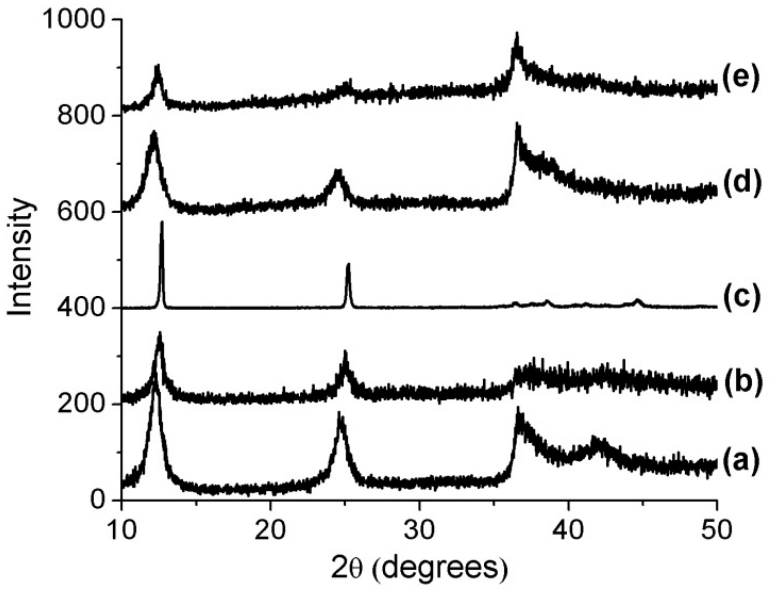

Figure 2.4: PXRD patterns for (a) K-δ-MnO_2 nanosheets, (b) K-δ-MnO_2 nanoparticles, (c) K-δ-MnO_2 micron-sized particles, (d) H-δ-MnO_2 nanosheets, and (e) H-δ-MnO_2 nanoparticles

The diffraction peaks for the micron-sized K-δ-MnO_2 particles synthesized at 800^{o}C are much narrower and sharper than the other two nanostructured samples, which is due to its highly crystalline nature. A small peak shift to high angle was also observed, indicating the shrinkage of interlayer distance in the micron particle. The crystallite size estimated from (001) peak using the Scherrer formula is 45.9 nm, which is significantly larger than the size of nanoparticles (14.8 nm) and in good agreement with SEM results (Figure 1). This is also witnessed as the surface area decreases 3-fold from 24.4 m^2/g (300^{o}C) to 8.1 m^2/g (800^{o}C).

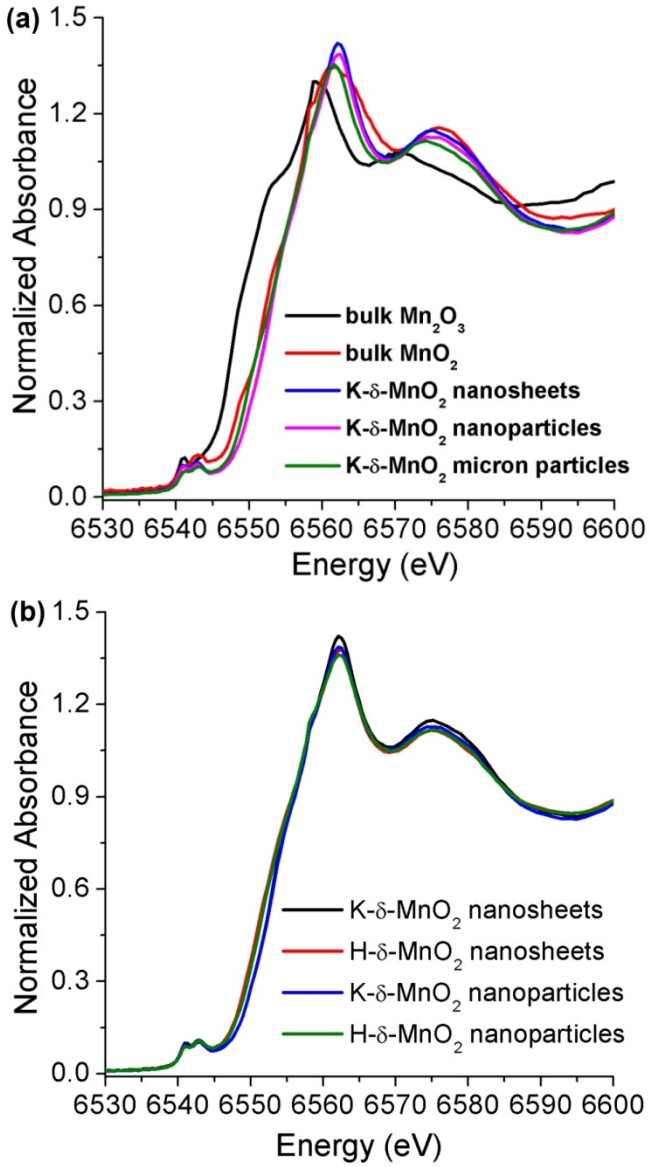

Figure 2.5: XANES data for (a) nanostructured and micron-sized K-δ-MnO_2 and (b) nanostructured H-δ-MnO_2

The oxidation states of manganese ions in all the δ-MnO_2 materials were examined by X-ray absorption near-edge structure (XANES) technique. The results are shown in Figures 2.5a and 2.5b. Two standard manganese oxides (MnO_2-Mn^{4+} and

Mn_2O_3-Mn^{3+}) are also presented for comparison. It is evident that the K-edges of Mn for all the K-containing δ-MnO_2 samples overlap the K-edge of bulk MnO_2, indicating the K-δ-MnO_2 samples have an average Mn oxidation state of 4+. Although it is expected that the insertion of alkaline cations into MnO_2 channels decreases the oxidation state of Mn due to the charge balance, the phenomenon observed in the K-containing δ-MnO_2 samples could be explained as the formation of oxygen-rich manganese oxide phases, which has also been reported in previous literature[7-9]. For the proton version of nanostructured δ-MnO_2, the XANES curves (Figure 2.5b) closely match the data for their potassium version counterparts, suggesting that the proton exchange process didn't affect the oxidation state of Mn in both nanostructures.

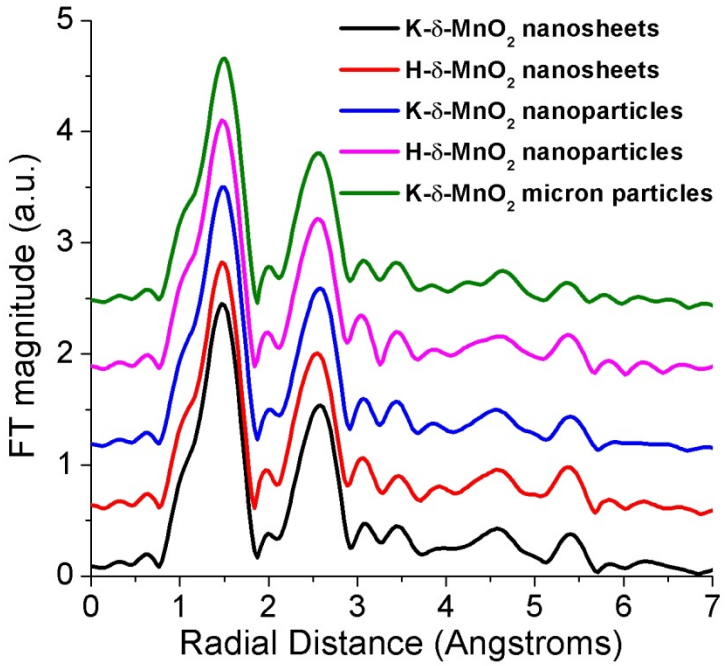

Figure 2.6: EXAFS data for all the δ-MnO_2 materials; curves are shifted along y-axis for display purpose

The crystal structures of all δ-MnO_2 samples were also investigated by the extended X-ray absorption fine structure (EXAFS) technique. R-space results presented in Figure 2.6 show that all the peaks match perfectly even at long radial distances, confirming that all the δ-MnO_2 samples have the same crystal structure, regardless of their morphologies, even after replacing all the potassium ions with protons. This is in good agreement with the PXRD analysis (Figure 2.4). The similarity in morphology, crystal structure, and oxidation state of Mn for K-δ-MnO_2 and H-δ-MnO_2 described above using multiple techniques is essential in exploring the role of alkaline cations in catalytic water oxidation.

Turning to photocatalytic water oxidation, the previously described $Ru^{2+}(bpy)_3$-$S_2O_8^{2-}$ sacrificial water oxidation system was utilized. The O_2 molecules thus generated are quantitatively analyzed using a gas chromatograph machine with a PDHID detector capable of detecting ppm levels of O_2. No increase in oxygen levels were detected when no light source was utilized or when the lamp was switched on but when no catalyst was employed. Similarly, no oxygen improvement was detected when no sensitizer $Ru^{2+}(bpy)_3$ was used. These control experiments clearly indicate that the observed increase in oxygen concentration when using the appropriate conditions is indeed photocatalytic in nature.

δ-MnO_2 Catalyst	TOF (s^{-1} per Mn)	BET (m^2/g)	TOF (s^{-1} per surface Mn)	Alkaline to Mn atomic ratio
K-δ-MnO_2 nanosheets	1.47E-5	35.7	5.20E-4	0.30
K-δ-MnO_2 nanoparticles	1.56E-5	24.4	8.04E-4	0.32
K-δ-MnO_2 micron particles	1.17E-5	8	1.84E-3	0.34
H-δ-MnO_2 nanosheets	1.00E-5	151	8.34E-5	0.02
H-δ-MnO_2 nanoparticles	8.45E-6	121.6	8.74E-5	0.02
Na-δ-MnO_2 nanosheets	9.40E-6	6	1.97E-3	0.31

Table 2.1: Oxygen production TOFs and BET surface areas of various δ-MnO_2 materials.

Photocatalytic water oxidation activities for all the catalysts are shown in Table 2.1. In order to investigate the potassium effort on the activity of manganese oxides in oxygen evolution, we carefully analyzed the K/Mn ratios by ICP-OES and EDX measurements, which confirm the K contents in all the catalysts (Table 2.1). All the δ-MnO_2 catalysts exhibited a similar TOF of 0.8-1.6×10^{-5} s^{-1} per Mn. In order to normalize the TOF by the surface area, the number of surface Mn atoms per m^2 had to be determined. Using the unit cell of length 5.149×7.176Å with 2 Mn atoms on a face, the density of surface Mn atoms was estimated to be 5.5×10^{18} atoms/m^2. By using BET surface area, we could obtain the TOF per surface Mn. The K-containing manganese oxides exhibit TOFs of 5-18×10^{-4} s^{-1} per surface Mn, about one order higher than their proton version counterparts. It is interesting to note that many previous reported manganese oxide based water oxidation catalysts have a very similar TOF per surface Mn, such as, 1×10^{-3} s^{-1} for λ-MnO_2 (LT), 8×10^{-4} s^{-1} for Mn oxides supported in mesoporous silica, and 7×10^{-4} s^{-1} $CaMn_2O_4$ catalyst[1, 10, 11].

Compared with proton-containing δ-MnO_2, the K-containing catalysts exhibit higher TOFs per surface Mn, although both nanostructured H-containing δ-MnO_2 samples have much larger surface areas than their potassium versions. The structural analysis, including PXRD, SEM, TEM, XANES and EXAFS, has demonstrated that the crystal structure was maintained throughout the proton exchange process, while the HRTEM data (Figure 2.3) suggest that the layered structure of H-δ-MnO_2 samples became less ordered compared to K-δ-MnO_2. This might be due to the exfoliation of MnO_2 layers during the proton exchange, leading to ultra-high surface areas. Although we should expect higher oxygen evolution activity from catalysts with larger surface area, it is clearly not the case in the present study. One possible explanation is that the surface area gained upon the removal of potassium cations can be accessed by only nitrogen molecules in the gas absorption experiment, but not $Ru^{2+}(bpy)_3$ sensitizer (a much larger molecule than N_2) in the photocatalytic oxygen evolution. Without $Ru^{2+}(bpy)_3$ sensitizer available on the catalyst surface, the catalytic sites (surface Mn) lose the capability to catalyze oxygen evolution from water under visible light. These results in Table 2.1 are in good agreement with our earlier work as the same set of alkali metal containing catalysts show similar TOF , independent of the catalyst's morphology[3].

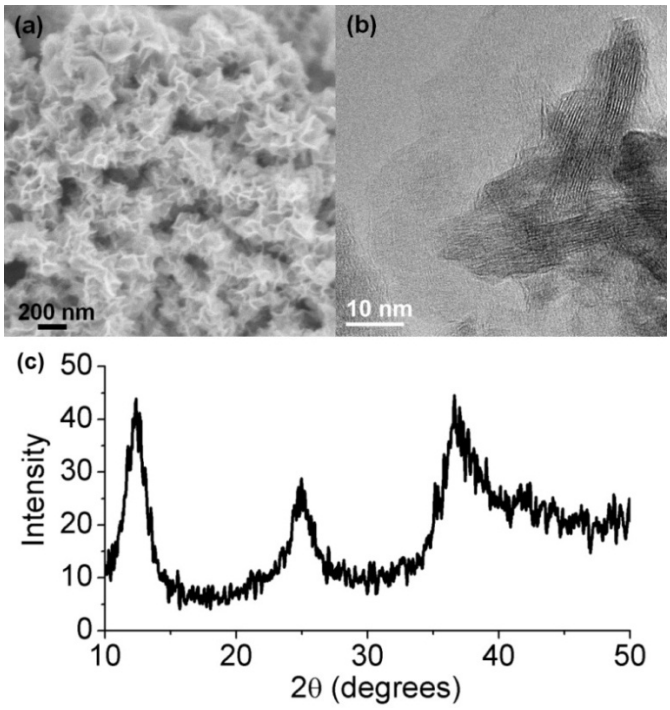

Figure 2.7: (a) SEM image, (b) HRTEM image, and (c) PXRD pattern for Na-δ-MnO_2 nanosheets

Further studies have been done to clarify the role of potassium in the photocatalytic oxygen evolution reaction. We synthesized Na-containing δ-MnO_2 nanosheets through a solution chemistry approach[8]. In a typical synthesis, an aqueous solution of manganese nitrate is added into a sodium hydroxide solution containing ~10% H_2O_2. After one hour reaction at room temperature, the resulting precipitate is recovered via centrifugation and washed with water. The SEM image (Figure 2.7a) shows that as-prepared Na-containing δ-MnO_2 has the nanosheet morphology, similar to the K-containing δ-MnO_2 sample. The nanosheets with an average particle size of 200-300 nm aggregated into large secondary particles (a few micron meters) with a poorly defined shape, while the K-δ-MnO_2 nanosheets form uniform and spherical

secondary particles (Figure 2.2a). The HRTEM image (Figure 2.7b) confirmed that the layered crystal structure of Na-δ-MnO_2 sample, in good agreement with PXRD result (Figure 2.7c). We investigated the oxygen evolution activity of this Na-δ-MnO_2 sample under identical conditions for K-containing samples. The oxygen evolution results (Table 2.1) clearly demonstrated that the Na-δ-MnO_2 catalyst exhibits a similar TOF per surface Mn compared to potassium version of δ-MnO_2, indicating that alkaline ions in both Na-δ-MnO_2 and K-δ-MnO_2 samples may not directly be involved into photocatalytic oxygen evolution, but stabilize the layered structure of δ-MnO_2. Such a finding is also consistent with our previous α-MnO_2 nanotube study, in which we discovered that the catalyst exhibited a similar TOF per Mn after aggressive acid treatment.[3]

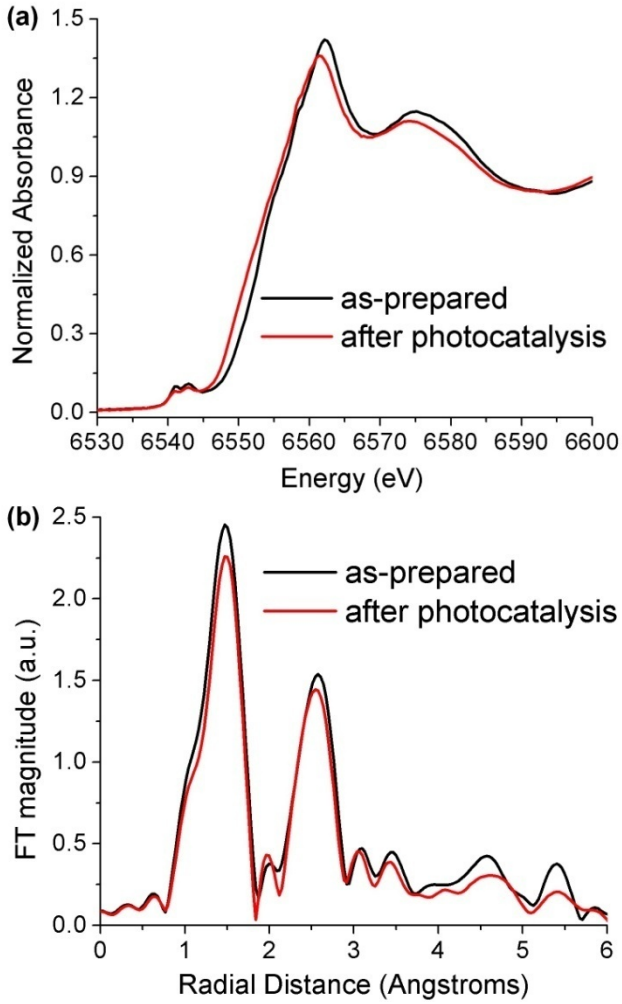

Figure 2.8: (a) XANES and (b) EXAFS results for K-δ-MnO_2 nanosheets and after photocatalytic water oxidation

As a critical characteristic, we proceeded to explore the stability of nanostructured alkaline containing δ-MnO_2 nanosheet catalyst. We recovered the catalyst after one hour photocatalytic oxygen evolution and re-examined them by SEM and XAS techniques. SEM images for the nanostructured K-δ-MnO_2 clearly show the morphology of the catalysts were maintained, while the EDX results indicate a partial

potassium content loss after photolysis (17.87 wt% to 6.56 wt%). Such a loss might be due to the proton exchange during the water oxidation reaction.

In order to determine if the potassium loss had an effect on the activity of the catalyst, stability tests were conducted. For these tests, the reactor was set up as described in the experimental section. The reactor was purged with helium and then sealed. An injection to the GC was made to serve as a baseline, and then the light was turned on. After 30 minutes of irradiation, another injection was made. After this injection, the pH of the reaction mixture was adjusted back to 5.8, another 130 mg of $Na_2S_2O_8$ was added to the reactor and the photolysis was run for another 30 minutes using the same catalyst. These steps were repeated one more time in order to get the third measurement. The TOF's observed in all 3 measurements were similar (see Table 2.2), which suggested that the potassium loss doesn't affect the TOF of K-δ-MnO_2 catalysts. The XANES and EXAFS data for K-δ-MnO_2 nanosheets are shown in Figure 2.8. After photocatalysis, a small shift of Mn K-edge to low energy was observed, which indicates a slight reduction of Mn oxidation state during the photocatalytic oxygen evolution. The EXAFS data for both before and after photocatalysis show almost identical patterns, confirming the crystal structural robustness during oxygen evolution, although at long radial distances, a slight reduction in peak intensities for the catalyst after photocatalysis was observed, which may suggest the decrease of long range atomic ordering. Overall, the K-δ-MnO_2 catalysts exhibit good structural stability and catalytic reproducibility.

δ-MnO_2 Nanosheet Catalyst	TOF (s^{-1} per Mn)
Fresh Catalyst	1.47E-5
Spent Catalyst – Run 1	1.63E-5
Spent Catalyst – Run 2	1.49E-5

Table 2.2: Oxygen production TOFs and BET surface areas of various δ-MnO_2 materials

2.4 Conclusions

K-containing δ-MnO_2 nanosheets and nanoparticles have been synthesized through hydrothermal reaction and solid state reactions. Their catalytic properties in water oxidation reaction driven by visible light have been studied for the first time. The role of alkaline cations in oxygen evolution has been explored through systematic comparison between K-containing δ-MnO_2 and proton-containing δ-MnO_2 with an identical morphology and crystal structure. The two nanostructured K-δ-MnO_2 catalysts exhibited approximately one order magnitude higher activities per surface site compared with proton-containing counterparts, although both nanostructured H-δ-MnO_2 catalysts have much larger surface areas. Such a phenomenon might be as the higher surface areas of nanostructured H-δ-MnO_2 catalysts cannot be accessed by the $Ru^{2+}(bpy)_3$ sensitizer. Also, a sodium-containing δ-MnO_2 with an identical crystal structure was synthesized and exhibited a similar TOF as the K-δ-MnO_2, suggesting that the alkaline cations are not directly involved into the catalytic water oxidation, while they stabilize the MnO_2 layers.

2.5 References

(1) Jiao, F.; Frei, H. *Chemical Communications* **2010**, *46*, 2920.

(2) Jiao, F.; Frei, H. *Angewandte Chemie-International Edition* **2009**, *48*, 1841.

(3) Boppana, V. B. R.; Jiao, F. *Chemical Communications* **2011**, *47*, 8973.

(4) Thackeray, M. M. *Progress in Solid State Chemistry* **1997**, *25*, 1.

(5) Ogata, A.; Komaba, S.; Baddour-Hadjean, R.; Pereira-Ramos, J. P.; Kumagai, N. *Electrochimica Acta* **2008**, *53*, 3084.

(6) Wang, X.; Li, Y. D. *Chemistry-a European Journal* **2003**, *9*, 300.

(7) Kim, S. H.; Kim, S. J.; Oh, S. M. *Chemistry of Materials* **1999**, *11*, 557.

(8) Prieto, O.; Del Arco, M.; Rives, V. *Journal of Materials Science* **2003**, *38*, 2815.

(9) Gaillot, A.-C.; Drits, V. A.; Manceau, A.; Lanson, B. *Microporous and Mesoporous Materials* **2007**, *98*.

(10) Najafpour, M. M.; Ehrenberg, T.; Wiechen, M.; Kurz, P. *Angewandte Chemie-International Edition* **2010**, *49*, 2233.

(11) Robinson, D. M.; Go, Y. B.; Greenblatt, M.; Dismukes, G. C. *Journal of the American Chemical Society* **2010**, *132*, 11467.

Chapter 3

EFFECT OF THE SUPPORT ON THE PHOTOCATALYTIC WATER OXIDATION ACTIVITY OF COBALT OXIDE NANOCLUSTERS

3.1 Introduction

It was recently reported the first example of cobalt oxide nanoclusters in a mesoporous silica support as efficient and robust catalysts[1]. Co_3O_4 nanoclusters embedded inside mesoporous silica SBA-15 support with two different loading levels (i.e. 4wt% and 8wt%) were obtained via wet impregnation method. The larger Co_3O_4 clusters (8 wt% sample) exhibit a somehow lower TOF of 0.5 $s^{-1}nm^{-2}$ compared with the TOF (1 $s^{-1}nm^{-2}$) of 35 nm diameter clusters (4 wt% sample). One interesting observation by comparing the TOFs of the nanostructured Co_3O_4 clusters in mesoporous silica SBA-15 with those of μm sized bare Co_3O_4 particles (no silica support) is that the O_2 yield per second is 1550 times larger for 35 nm clusters in SBA-15 than for micron sized Co_3O_4 particles if normalized to the same weight. Even after normalizing the TOFs using the number of surface atoms (96 times difference), the activity for Co_3O_4 nanoclusters supported in SBA-15 is still 16 times higher that of bare Co_3O_4 micron particles. Our speculation of the original of additional 16 times difference is that mesoporous silica support may promote the activities of surface cobalt atoms possibly by suppressing surface restructuring. The silica support may also assist deprotonation during photocatalysis, and thus enhances the proton diffusion and improves the kinetics of the catalytic sites.

In order to further elucidate the role of support in photocatalytic water oxidation, we investigated the photocatalytic activity of cobalt oxide nanoparticles with different SiO_2 or γ-Al_2O_3 supports in this paper. Two mesoporous silica supports, SBA-15 and KIT-6, were synthesized and loaded with Co_3O_4 nanoclusters inside their channels using bi-solvent and wet-impregnation methods. The resulting catalysts were systematically investigated as multi-electron oxygen evolution catalysts in a well-established $Ru^{2+}(bpy)_3$-$Na_2S_2O_8$ system to explore how the supports affect the photocatalytic activities.

3.2 Experimental Methods

3.2.1 Synthesis of mesoporous silica KIT-6

The synthesis of mesoporous silica KIT-6 was previously reported by Kleitz and his co-workers[2]. 20 g of tri-block copolymer P123 (Sigma Aldrich, M_n ~5800) was dissolved in a mixture of 750 mL of deionized H_2O and 34 mL of HCl (Sigma Aldrich, 37wt%). Then, 20 g of 1-butanol (Sigma Aldrich, 99.8%) was added and the mixture was stirred at 34°C for one hour. After that, 43 g of tetraethyl orthosilicate (TEOS, Sigma Aldrich, 98%) was added and the mixture was stirred for 24 hours at 34°C. The resulted mixture was transferred into polypropylene bottles, sealed, and undergone hydrothermal treatment at 100°C for another 24 hours. After hydrothermal treatment, the mixture was filtered and treated with a mixture composed of 30 mL of HCl and 300 mL of ethanol, and washed with DI water. The resulting powder was dried and calcinated at 550°C for 3 hours in air at a ramp rate of 2°C/min to remove the polymer template.

3.2.2 Synthesis of mesoporous silica SBA-15

The synthesis of mesoporous silica SBA-15 was previously reported by Zhao and his co-workers[3]. 20 g of tri-block copolymer P123 (Sigma Aldrich, M_n ~5800) was added to a mixture of 750mL of deionized H_2O and 40 mL of 37 wt% HCl. Once fully dissolved, 44 g of TEOS was added and the mixture was stirred at 40°C for 24 hours. The mixture was then transferred into polypropylene bottles, sealed, and maintained at 100°C for another 24 hours. After that, the mixture was filtered, washed with DI water, dried and calcinated at 500°C for 3 hours with a ramp rate of 2°C/min.

3.2.3 Synthesis of mesoporous silica supported Co_3O_4 catalysts

The cobalt content in the final catalyst is set to 4% by weight as an optimal loading according to our previous findings in Co_3O_4 loaded SBA-15 catalysts[1]. Two different methods were used to load cobalt onto the mesoporous silica supports: wet impregnation and bi-solvent[4-6]. For wet impregnation, 0.208 g of $Co(NO_3)_2 \cdot 6H_2O$ (7.17×10^{-4} mol Co, Sigma Aldrich, 98%) was dissolved in 2 mL of ethanol. The solution was added to 1 g of mesoporous silica (SBA-15 or KIT-6) dropwise, followed by drying at 60°C. For the bi-solvent method, 1 g of mesoporous silica support was dispersed in 20 mL of either hexane (Alfa Aesar, environmental grade) or pentane (Sigma Aldrich, 98%). 1 mL of an aqueous solution of $Co(NO_3)_2 \cdot 6H_2O$ (containing 7.17×10^{-4} mol Co) was added dropwise to the silica dispersion under stirring. After stirring for another one hour, the mixture was filtered and dried at 60°C. To convert the cobalt precursor to Co_3O_4, all dried samples were heated in air to 700°C at a ramp rate of 2°C/min. Once 700°C was reached, the samples were cooled naturally to room temperature.

3.2.4 Synthesis of nanoparticle supported Co_3O_4 catalysts

Two different nanoparticles, SiO_2 and Al_2O_3, were used as support to study the influence of support composition on photocatalytic oxygen evolution from water. Both nanoparticle supports were obtained from Sigma Aldrich (SiO_2: LUDOX TM-40, 420786 and Al_2O_3: nanopowder, 718475). SiO_2 and Al_2O_3 nanoparticles have average particle diameters of 25±3 nm and 13 nm, respectively. The Co_3O_4 nanoparticles were synthesized according to a previously published procedure[7]. 0.50 g of $Co(CH_3COO)_2 \cdot 4H_2O$ was dissolved in 2.0 ml of DI water and 23.0 ml of ethanol in a 40mL Teflon liner. 2.5 ml of 28% ammonia was added to the cobalt solution and stirred for 10 minutes. The liner was inserted into an autoclave and heated at 150°C for 3 hours. After heat treatment, the autoclave was cooled to room temperature and the product was washed with DI water through centrifugation-redispersion. The final product was then dried at 60°C overnight. In a typical cobalt loading, 0.02 g of as-made Co_3O_4 nanoparticles was dispersed in 15 mL of methanol and the resulted solution was added to either 0.85 g of LUDOX TM-40 solution (40% SiO_2) or 0.34 g of Al_2O_3 nanoparticles. The mixture was stirred in a fume hood overnight until a dried powder was obtained. Finally, the powders were heated in air at 200°C for 1h to obtain the product (~4wt% Co loading).

3.2.5 Structural Characterization

All Powder X-Ray Diffraction (PXRD) measurements were performed with a Rigaku Ultima IV Diffractometer using Cu *K*α radiation. Transmission electron microscopy (TEM) was performed with a JEOL JEM-2010F field-emission transmission electron microscope, using an accelerating voltage of 200 kV. Surface

Area, pore size and pore volume measurements were performed using an isothermal nitrogen adsorption/desorption instrument. Inductively Coupled Plasma Optical Emission Spectrometry (ICP-OES) analysis was carried out in the Soil Lab at the University of Delaware.

3.2.6 Photocatalytic oxygen evolution from water

Photochemical water oxidation experiments were conducted in a 100 mL reactor containing 40 mL of aqueous buffer (Na_2SiF_6-$NaHCO_3$) at pH 5.8, 390 mg Na_2SO_4, 130 mg $Na_2S_2O_8$, and 75 mg of the as-synthesized catalyst. The amount of $[Ru(bpy)_3]Cl_2 \cdot 6H_2O$ sensitizer added to the reactor was varied in the range of 20-100mg to determine the optimal ratio between catalyst and sensitizer. The light source is a 300W Xe research lamp (UV fused silica, 1.3in collimated, F/1, 1.5inch) with 400 nm cut-off filter. The resulting O_2 molecules in the head space were quantitatively analyzed by a Shimadzu gas chromatography system (Shimadzu GC-2014) equipped with a PDHID detector. All the experiments were conducted at room temperature (~ 25^oC). A base-line was recorded for each experiment to confirm no leakage in the system.

3.3 Results and Discussion

In our previous study, we have reported the preparation of Co_3O_4 nanoclusters supported in mesoporous silica SBA-15 through a wet-impregnation method. SBA-15 consists of one-dimensional (1D) channels with a hexagonal symmetry.[3] The average pore diameter of main channels is approximate 7-8 nm and the main channels are interconnected via micropores (1-2 nm in diameter). The cobalt oxide cluster formed

inside the channels of SBA-15 replicated its pore structure, resulting in a bundle-like morphology. Here, we choose mesoporous silica (KIT-6) as the catalyst support, which has bi-continuous three-dimensional (3D) pores throughout the whole particle.[2] With such 3D pores, KIT-6 as a catalyst support offers a better accessibility for reagents to reach the surface of Co_3O_4 clusters (catalytic site for water evolution).

A KIT-6/Co_3O_4 catalyst was firstly synthesized using a wet impregnation method (denoted as KIT-6/Co_3O_4-WI). To confirm the success of Co_3O_4 cluster formation inside the mesopores of KIT-6, TEM analysis was performed and a typical image of KIT-6/Co_3O_4-WI is shown in Figure 3.1a. The dark dots in the image represent the cobalt oxide particles. Clearly, cobalt oxide nanoclusters were successfully loaded into the channels of KIT-6 and no large particle of cobalt oxide was formed outside the channels. It can also be seen from Figure 3.1a that the Co_3O_4 cluster sizes in KIT-6/Co_3O_4-WI have a wide distribution from 30 nm to 200 nm.

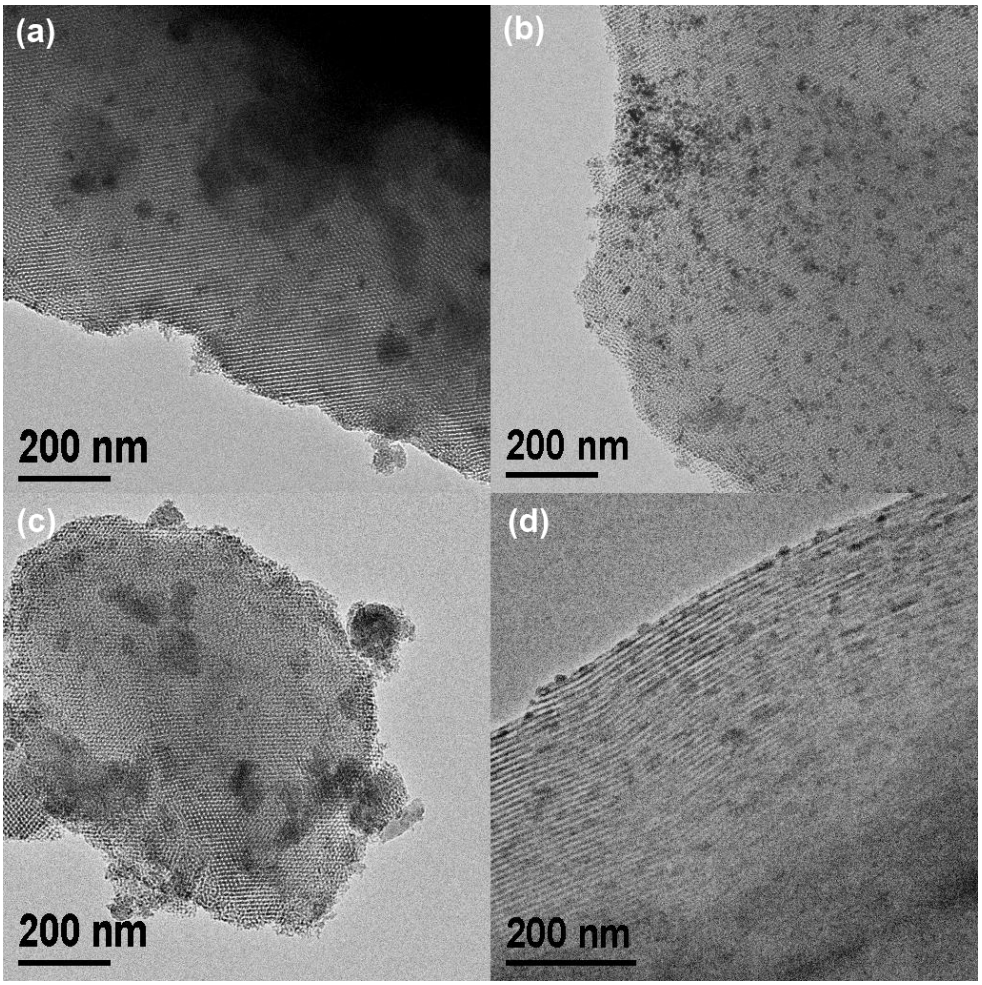

Figure 3.1: TEM images for (a) KIT-6/Co_3O_4, (b) KIT-6/Co_3O_4-HEX, (c) KIT-6/Co_3O_4-PEN, and (d) SBA-15/Co_3O_4-HEX

To prepare smaller clusters with a narrow size distribution, the bi-solvent method, which has been reported to be an effective approach to load metal precursor into the hydrophilic silica channels was employed.[5, 6] Here, we chose hexane and pentane as non-polar solvents and the resulting catalysts are denoted as KIT-6/Co_3O_4-HEX and KIT-6/Co_3O_4-PEN, respectively. The morphologies of as-prepared KIT-6/Co_3O_4-HEX and KIT-6/Co_3O_4-PEN were examined by TEM. It can be seen from the

TEM images (Figures 3.1b and 3.1c) that KIT-6/Co_3O_4-HEX contains very small Co_3O_4 nanoclusters (below 25 nm) with a narrow size distribution, while the clusters in KIT-6/Co_3O_4-PEN are much bigger (~50-200 nm) and Co_3O_4 particles formed outside the pores were also observed. The TEM results confirm that hexane is a better choice than pentane for small cluster formation in the bi-solvent method, although in a previous report the authors claimed that pentane is more effective over hexane.[6]

Following this finding, we synthesized a mesoporous silica SBA-15 version of catalyst (SBA-15/Co_3O_4-HEX) through the bi-solvent method using hexane as the non-polar solvent to make comparison with KIT-6/Co_3O_4-HEX. Because KIT-6 has a similar pore dimension as SBA-15 (approximately 7-8 nm) and its main channels are interconnected via small pores (1-2 nm) as well, a detailed comparison between SBA-15/Co_3O_4-HEX and KIT-6/Co_3O_4-HEX allows us to investigate how the pore dimension of silica support (*i.e.* 1D *vs* 3D) affects the activity of Co_3O_4 clusters. A typical TEM image of SBA-15/Co_3O_4-HEX is shown in Figure 3.1d and well-dispersed small clusters can be clearly observed. Based on TEM analysis, the statistical sizes of Co_3O_4 clusters are summarized in left column of Table 3.1.

Catalyst	Average Cluster Size (nm)	Crystallinity size (nm)
KIT-6/Co_3O_4-WI	51	10
KIT-6/Co_3O_4-HEX	25	8
KIT-6/Co_3O_4-PEN	142	15
SBA-15/Co_3O_4-HEX	30	11

Table 3.1: Average cluster sizes estimated from TEM data and crystallinity sizes calculated from the Scherrer formula for all catalysts

Silica supports are confirmed to maintain highly ordered mesostructures in all the catalysts via TEM (Figure 3.1) as well as low angle powder X-ray Diffraction (PXRD) (Figure 3.2a) analysis. For the samples using KIT-6 as support, two low angle diffraction peaks at 0.97º and 1.12º corresponding to [211] and [200] diffractions plus one broad peak at ~1.7º were observed, indicating that well-ordered mesoporous structure of KIT-6 was preserved throughout the whole sample preparation procedure. For SBA-15/Co_3O_4-HEX, the PXRD pattern shows a sharp peak at 0.92º and two well-defined peaks at 1.58º and 1.82º, confirming the presence of ordered mesostructure with a hexagonal symmetry. The low angle PXRD results are in good agreement with the TEM data.

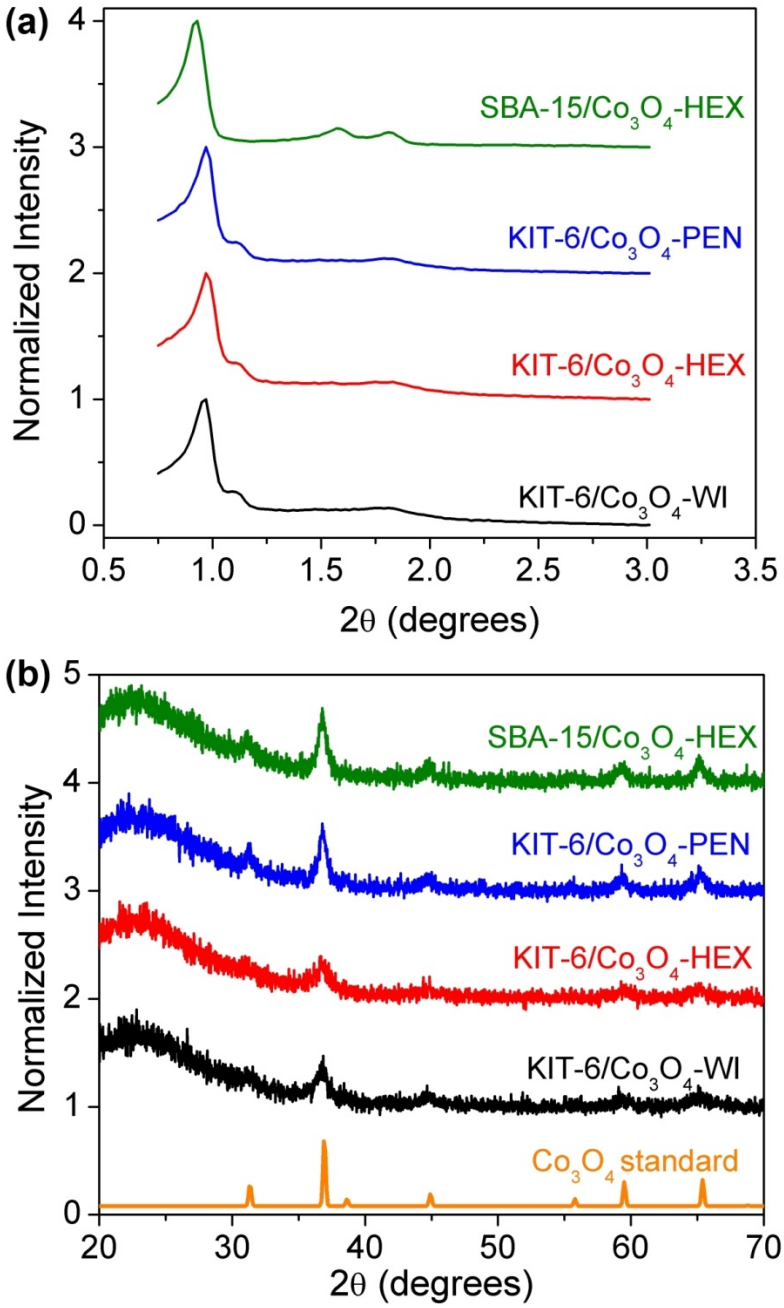

Figure 3.2: (a) Low angle and (b) high angle PXRD patterns for KIT-6/Co_3O_4-WI, KIT-6/Co_3O_4-HEX, KIT-6/Co_3O_4-PEN, and SBA-15/Co_3O_4-HEX. A standard PXRD pattern for bulk Co_3O_4 is also shown in (b) for comparison

Turning to the atomic level structure of the as-made catalysts, high angle PXRD analysis was used as a standard technique to determine the crystal structures of cobalt oxide particles formed inside the silica supports. High angle PXRD patterns for all the as-made samples are shown in Figure 3.2b and several diffraction peaks can be clearly observed, which closely match the standard PXRD pattern for bulk Co_3O_4 spinel. These results confirmed that cobalt oxide nanoclusters in all the samples have an identical Co_3O_4 spinel structure, regardless of the geometry of supports and synthetic methods. A broad peak at 22-23º is observed and it may be resulted from the amorphous silica support. The diffraction peaks in Figure 3.2b are significantly broadened, suggesting the nanocrystalline nature of Co_3O_4 spinel in these samples. The Scherrer formula was used to estimate the crystallinity size of Co_3O_4 and the results are listed in Table 3.1. Because the diffraction peaks for all the samples are poorly defined, the calculated crystallinity domain size for each sample in Table 3.1 is only a rough estimate. For KIT-6/Co_3O_4-WI, KIT-6/Co_3O_4-HEX, and SBA-15/Co_3O_4-HEX, the estimated crystal domain sizes closely match the pore dimension of mesoporous silica supports (7-8 nm), suggesting that the Co_3O_4 nanoclusters are well confined in the channels of mesoporous supports. However, KIT-6/Co_3O_4-PEN has an estimated crystal domain size of 15 nm, larger than the pore dimension. It is likely due to some of the large Co_3O_4 particles formed outside the mesopores (Figure 3.1c).

Photocatalytic water oxidation experiments were carried out using the $Ru^{2+}(bpy)_3$-$S_2O_8^{2-}$ system in an aqueous buffer (Na_2SiF_6-$NaHCO_3$) at pH 5.8. Control tests were performed to confirm that when any one of the three main components of this system (sensitizer, light source, and catalyst) was missing, no O_2 evolution could be observed.

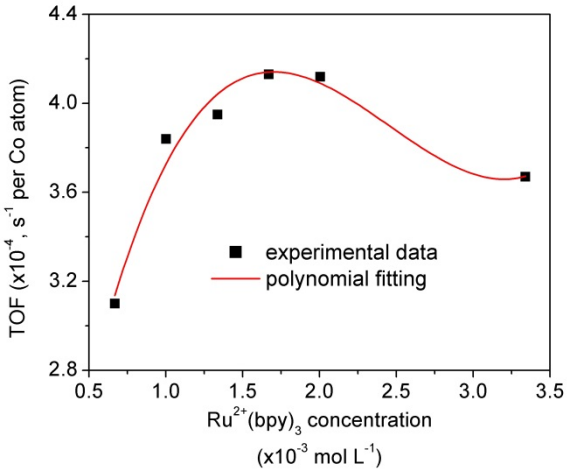

Figure 3.3 Sensitizer-TOF relationship using KIT-6/Co_3O_4-HEX as the catalysts

A series of experiments was performed to determine the optimal sensitizer concentration by fixing the catalyst weight at 75 mg and changing the concentration of $Ru^{2+}(bpy)_3$ from 6.7×10^{-4} mol·L^{-1} to 3.3×10^{-3} mol·L^{-1}. KIT-6/Co_3O_4-HEX was used as a standard catalyst in this study because of its small particle size and narrow size distribution. After 30 minutes of visible light radiation (300W, >400 nm), oxygen concentration in the head space was measured using GC. The turnover frequencies (TOFs) per Co atom was calculated from the oxygen yield and the results are plotted in Figure 3.3. As the concentration of $Ru^{2+}(bpy)_3$ increased, the TOF increased to reach a peak and then decreased. The decrease of TOF at high sensitizer concentration is caused by a "shielding" effect, which was also observed in the IrO_2 system[8]. When the concentration of $Ru^{2+}(bpy)_3$ is too high, a significant amount of incident photons will be absorbed by the free $Ru^{2+}(bpy)_3$ molecules in the solution and therefore less photons can be accessed for the sensitizer molecules on the catalyst surface, resulting in a low oxygen evolution rate. An optimal $Ru^{2+}(bpy)_3$ concentration of ~1.7×10^{-3}

$mol \cdot L^{-1}$ is estimated from a polynomial fitting and all the remaining oxygen evolution experiments were performed at the optimal concentration to achieve a maximum of oxygen evolution rate.

In order to investigate intrinsic activity of catalyst, the whole water oxidation cycle (Figure 1.2) has to be limited by the rate of oxygen molecule formation on the catalyst surface. To confirm that, we varied the amount of sodium persulfate in the system and the same initial oxygen evolution rate was observed, confirming that the electron transfer from sensitizer to persulfate (sacrificial electron acceptor) is not the rate-limiting step. After that, another control experiment at an identical condition, except using only half amount of the catalyst, was performed. The oxygen yield was reduced by 50% with half amount of the catalyst, confirming that catalytic reaction on the surface of catalyst is the rate-limiting step in our system.

Catalyst	Cobalt content (wt%)	O_2 yield ($\mu mol \cdot h^{-1}$)	TOF (s^{-1} per Co atom)
KIT-6/Co_3O_4-WI	3.8	57.1	3.3×10^{-4}
KIT-6/Co_3O_4-HEX	3.7	70.5	4.1×10^{-4}
KIT-6/Co_3O_4-PEN	3.8	36.7	2.1×10^{-4}
SBA-15/Co_3O_4-HEX	4.0	62.8	3.4×10^{-4}

Table 3.2: TOF's for all supported catalysts. 75mg of catalyst and 50mg of $Ru^{2+}(bpy)_3$ used for all measurements.

The oxygen yields for KIT-6/Co_3O_4-WI, KIT-6/Co_3O_4-PEN, and SBA-15/Co_3O_4-HEX that were measured using 75 mg of catalyst and 50 mg of $[Ru(bpy)_3]Cl_2 \cdot 6H_2O$ (i.e. $Ru^{2+}(bpy)_3$, 1.7×10^{-3} $mol \cdot L^{-1}$) are listed in Table 3.2. The accurate cobalt loading in each sample was confirmed by ICP-OES analysis, which is in agreement with the estimated value (~4 wt% Co). In 30 minutes of visible light

radiation, the KIT-6/Co_3O_4-HEX exhibited the highest rate of O_2 evolution from water (70.5 $\mu mol \cdot h^{-1}$), while the KIT-6/Co_3O_4-PEN catalyst showed a much lower rate (36.7 $\mu mol \cdot h^{-1}$). We attribute such a difference in oxygen evolution activities to their cluster sizes in the KIT-6 support. From the TEM and high angle PXRD data, it is clear that KIT-6/Co_3O_4-PEN has a much larger cluster size and crystallinity domain size, when compared with KIT-6/Co_3O_4-HEX. Difference in cluster sizes results in a different amount of surface catalytic sites that are available for photocatalytic water oxidation in both samples. The sample obtained from wet impregnation method has a medium cluster size (70 nm) and exhibits a TOF of 3.27×10^{-4} s^{-1} per Co atom, higher than that of KIT-6/Co_3O_4-PEN but lower than that of KIT-6/Co_3O_4-HEX. This observed TOF is consistent with our expectation based on structural characterization results (Table 3.1). Turning to SBA-15/Co_3O_4-HEX, it exhibits a TOF of 3.38×10^{-4} s^{-1} per Co atom, which is lower than that of KIT-6/Co_3O_4-HEX but close to that of KIT-6/Co_3O_4-WI. Because SBA-15/Co_3O_4-HEX has a similar particle size as KIT-6/Co_3O_4-HEX, it is concluded that such an increase in TOF for KIT-6/Co_3O_4-HEX is mainly due to the 3D porous support (KIT-6), which offers a better accessibility than 1D channels of SBA-15.

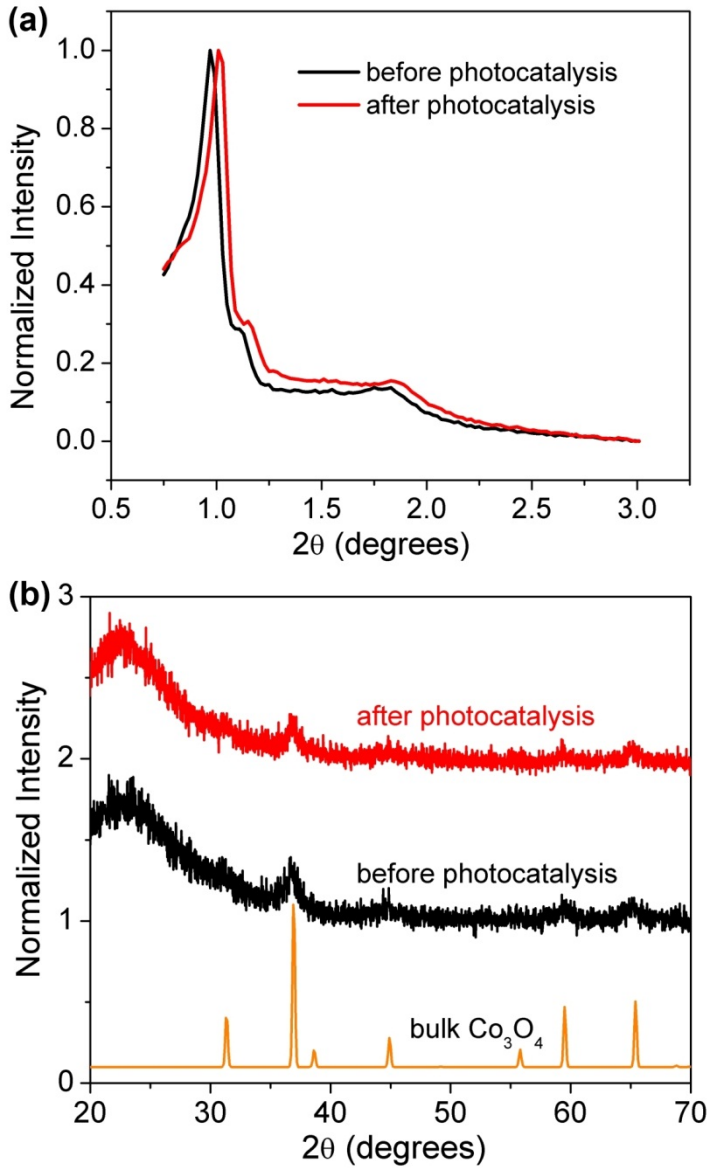

Figure 3.4: Low and high angle PXRD patterns for KIT-6/Co_3O_4-HEX before and after photocatalysis.

Superior stability of Co_3O_4 nanoclusters embedded in mesoporous silica support has been demonstrated in our previous work.[1] Here, we also investigated the preservation of ordered mesoporous structure of the support and the crystal structure

of Co_3O_4 clusters before and after photocatalytic reaction. The low angle PXRD patterns for KIT-6/Co_3O_4-HEX before and after one hour photolysis are displayed in Figure 3.4a, which clearly demonstrates that the ordered mesoporous structure of KIT-6/Co_3O_4-HEX was preserved after photocatalytic water oxidation. The high angle PXRD patterns (Figure 3.4b) confirm that the cobalt oxide clusters in KIT-6/Co_3O_4-HEX after reaction maintained their Co_3O_4 spinel structure.

One question that has not yet been answered is the role of silica in the photocatalytic oxygen evolution from water. As we noticed from previous work, there is still a factor of 16 times difference in oxygen evolution activity, which cannot be explained simply by the surface area of Co_3O_4 nanoclusters.[1] Our speculation is that the curved mesoporous silica channels may help suppress surface active site restructuring and assisting in the depronation process. To test this hypothesis, well-defined Co_3O_4 nanoparticles (diameter: ~6 nm) were used as model catalysts and loaded onto two different nanoparticulate supports, SiO_2 and Al_2O_3 (denoted as nano-SiO_2/Co_3O_4 and nano-Al_2O_3/Co_3O_4, respectively). The detailed procedure for sample preparation is described in the experimental section.

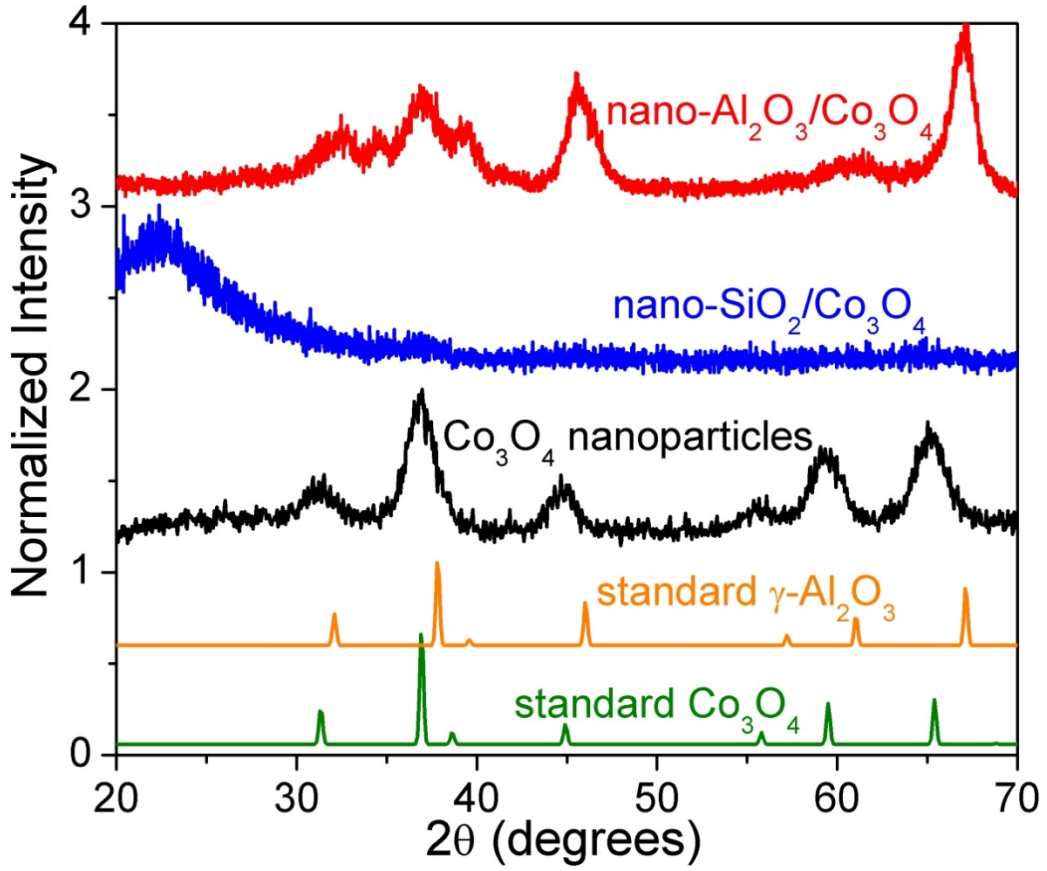

Figure 3.5: PXRD patterns for as-prepared Co_3O_4 nanoparticles, nano-SiO_2/Co_3O_4 and nano-Al_2O_3/Co_3O_4

Detailed structural characterizations were performed for all the as-prepared samples before photocatalytic studies. The as-prepared Co_3O_4 nanoparticles show clear diffraction peaks (Figure 3.5), closely matching the standard Co_3O_4 with a spinel structure. After loading Co_3O_4 nanoparticles (~4 wt% in final product) onto SiO_2 and γ-Al_2O_3 supports, none of the diffraction peaks for the Co_3O_4 spinel phase could be observed (Figure 3.5), due to the low concentration of Co_3O_4 in the final catalysts. Typical TEM images for the three catalysts are shown in Figure 3.6. It is evident that as-prepared Co_3O_4 nanoparticles have a spherical shape and a particle size of 6±2 nm

with a narrow distribution (Figure 3.6a). The lattice fringes of Co_3O_4 nanoparticles can be clearly observed in the HRTEM image (Figure 3.6b) and the observed distance between two lattice fringes is approximate 0.20 nm, which matches the distance between [400] planes in the Co_3O_4 spinel structure. For the nano-SiO_2/Co_3O_4, it is hard to distinguish the Co_3O_4 nanoparticles from SiO_2 at low magnification, while at high magnifications we clearly observed the lattice fringes with a distance of 0.28 nm that matches the d-space for [220] planes of Co_3O_4 spinel (Figure 3.6c-d). For the, nano-Al_2O_3/Co_3O_4 catalyst (Figures 3.6c-d) it is difficult to distinguish the Al_2O_3 particles from the Co_3O_4 particles since both have a crystalline structure, but no large particle was observed in any of these samples, indicating that most of the nanoparticles are well dispersed throughout the catalysts.

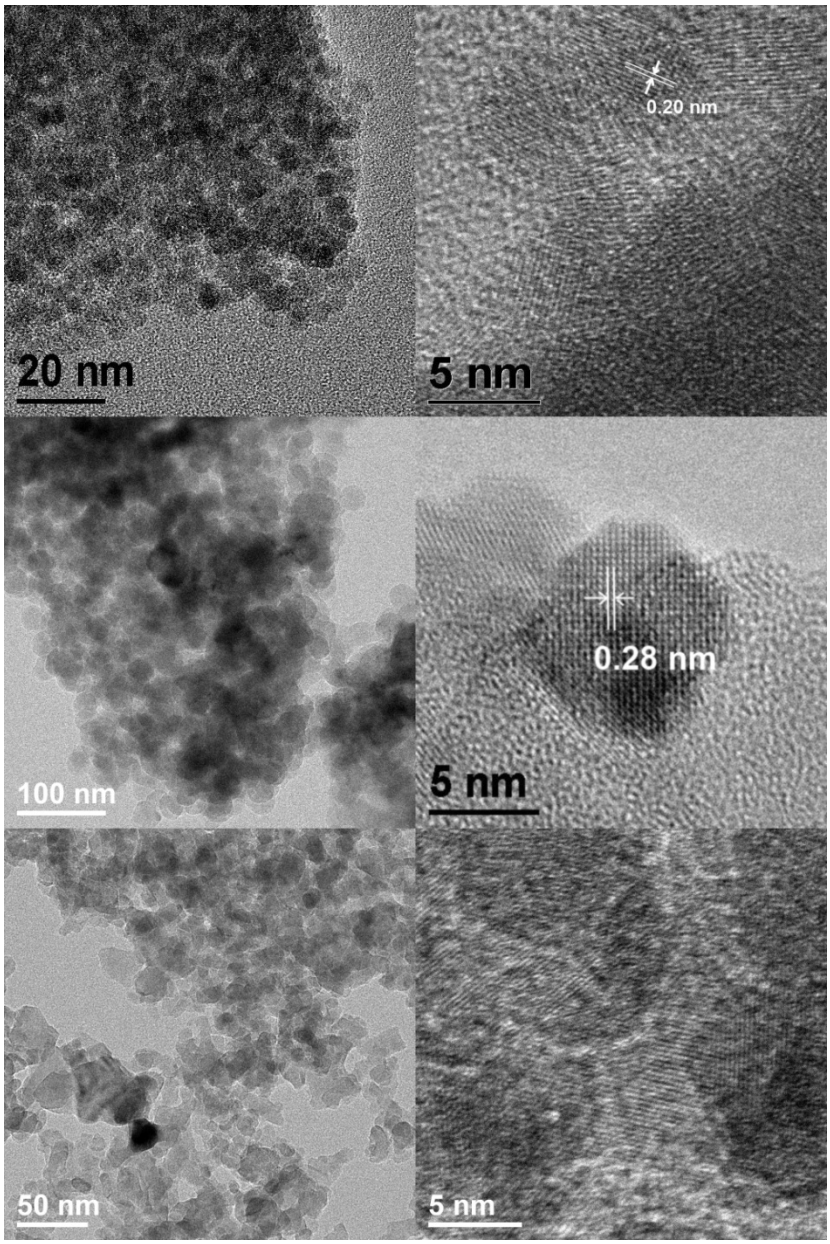

Figure 3.6: TEM and HRTEM images for (top) as-made Co_3O_4 nanoparticles, (middle) nano-SiO_2/Co_3O_4, and (bottom) nano-Al_2O_3/Co_3O_4

Photocatalytic water oxidation experiments were performed using two catalysts with a nanoparticulate support and the same amount of Co loading. The other

conditions were fixed at the same amount as those used in previous studies. The results are summarized in Table 3.3. The bare Co_3O_4 nanoparticles exhibited a TOF of 2.5×10^{-4}, which is lower than two supported catalysts. In addition, it can be seen that nano-Al_2O_3/Co_3O_4 exhibited a 26% higher oxygen evolution activity than that of nano-SiO_2/Co_3O_4. The reason why nano-Al_2O_3/Co_3O_4 is more active is likely due to the fact that the surface area of Al_2O_3 (~140 m^2g^{-1}) is larger than that of SiO_2 (~100 m^2g^{-1}), resulting in a better physical separation of Co_3O_4 nanoparticles. Such a physical separation is essential to avoid active site aggregation, as it was shown in the control experiment that pure Co_3O_4 nanoparticles exhibited a much lower activity as oxygen evolution catalyst than supported catalysts under identical conditions (Table 3.3). Considering that a 26% difference in activity is not significant, it is less likely that either SiO_2 or Al_2O_3 support is directly involved in the enhancement of water oxidation activity. Therefore, we conclude that the role of support in the photocatalytic reaction is physical separation and immobilization of catalytic particles to avoid aggregation.

Catalyst	Cobalt content (wt%)	O_2 yield ($\mu mol\cdot h^{-1}$)	TOF (s^{-1} per Co atom)
nano-SiO_2/Co_3O_4	4.0	66.8	3.25×10^{-4}
nano-Al_2O_3/Co_3O_4	4.0	84.3	4.6×10^{-4}
Co_3O_4 nanoparticles	4.0	46.6	2.5×10^{-4}

Table 3.3: Photocatalytic oxygen evolution results for nanoparticle supports

3.4 Conclusion

We have successfully synthesized a range of Co_3O_4 nanoclusters supported by various substances, including mesoporous silica KIT-6, mesoporous silica SBA-15, SiO_2 nanoparticles, and γ-Al_2O_3 nanoparticles. A bi-solvent method was used to obtain

a high quality catalyst with all the Co_3O_4 nanoclusters formed inside the mesoporous support through a hydrophilic-hydrophobic interaction. Hexane has been proved to be a better non-polar solvent in the bi-solvent approach than pentane, and the resulting catalyst consists of Co_3O_4 nanoclusters with a small particle size and narrow size distribution. Photocatalytic water oxidation activities of as-synthesized catalysts were investigated using the $Ru^{2+}(bpy)_3$-persulfate system. The results confirmed that smaller Co_3O_4 cluster size, higher water oxidation activity. Compared to SBA-15, KIT-6 was found to be a better support, which is likely due to its 3D porous structure offering a more accessible system. To elucidate the role of support in the photocatalytic oxygen evolution, we compared bare Co_3O_4 nanoparticles with supported ones. Although both SiO_2 and γ-Al_2O_3 supported catalysts exhibited higher activities than bare nanoparticles, switching from SiO_2 to γ-Al_2O_3 didn't influence their activity in a significant way, indicating that the composition and surface atoms of the support are not the critical factors. The key role of the support in photocatalytic water oxidation reaction is to physically separate and immobilize the Co_3O_4 nanoclusters. This makes the morphology of the support the most critical factor in these catalysts as it will determine the size and accessibility of the nanoclusters.

3.5 References

(1) Jiao, F.; Frei, H. Angewandte Chemie-International Edition **2009**, 48, 1841.

(2) Kleitz, F.; Choi, S. H.; Ryoo, R. Chemical Communications **2003**, 2136.

(3) Zhao, D. Y.; Feng, J. L.; Huo, Q. S.; Melosh, N.; Fredrickson, G. H.; Chmelka, B. F.; Stucky, G. D. Science **1998**, 279, 548.

(4) Jiao, F.; Bruce, P. G. Adv. Mater. **2007**, 19, 657.

(5) Yen, H.; Seo, Y.; Guillet-Nicolas, R.; Kaliaguine, S.; Kleitz, F. Chem. Commun. **2011**, 47, 10473.

(6) van der Meer, J.; Bardez, I.; Bart, F.; Albouy, P. A.; Wallez, G.; Davidson, A. Microporous Mesoporous Mater. **2009**, 118, 183.

(7) Dong, Y. M.; He, K.; Yin, L.; Zhang, A. M. Nanotechnology **2007**, 18.

(8) Hara, M.; Waraksa, C. C.; Lean, J. T.; Lewis, B. A.; Mallouk, T. E. Journal of Physical Chemistry A **2000**, 104, 5275.

Chapter 4

CONCLUSIONS AND PRELIMINARY WORK ON CARBON DIOXIDE REDUCTION CATALYSTS

4.1 Conclusions

In this thesis, manganese and cobalt oxide water oxidation catalysts were synthesized and tested for photocatalytic H_2O oxidation activity in the $Ru^{2+}(bpy)_3$-$S_2O_8^{2-}$ system using only visible light. Multiple nanostructured, δ-MnO_2 catalysts containing different alkaline cations were synthesized. A systematic comparison between K-containing δ-MnO_2 and proton-containing δ-MnO_2 with an identical crystal structure was done in order to determine that effect of K^+ ions. The K-δ-MnO_2 catalysts had TOF's about one order of magnitude higher than their H-δ-MnO_2 counterparts, even though the H-δ-MnO_2 catalysts have much larger surface areas. One possible reason for this observation is that the $Ru^{2+}(bpy)_3$ sensitizer was too large to access all the sites on the H-δ-MnO_2 catalysts A sodium-containing δ-MnO_2 with an identical crystal structure was also synthesized and exhibited a similar TOF as the K-δ-MnO_2, suggesting that the cations stabilize the MnO_2 layers.

To explore the effect of the support material on cobalt oxide H_2O oxidation catalysts, supported and unsupported Co_3O_4 nanoparticles were synthesized. A bi-solvent method was used to obtain a high quality catalyst consisting of Co_3O_4 nanoclusters supported by mesoporous silica. It was found that the hexane/water combination was better than the pentane/water approach. The hexane/water approach resulted in a catalyst consisting of Co_3O_4 nanoclusters with a small particle size and

narrow size distribution while the pentane/water approach yielded clusters that were outside the pores of the mesoporous silica. It was found that as the Co_3O_4 cluster size became smaller, the water oxidation activity increased and that KIT-6 was the optimal support due to its 3D pores structure making the Co_3O_4 clusters more accessible than the 1D pores of SBA-15. Bare Co_3O_4 nanoparticles were also studied with supported particles so that the role of support could be determined. Both SiO_2 and γ-Al_2O_3 supported catalysts exhibited TOF's than bare nanoparticles, but there were no significant difference between SiO_2 and γ-Al_2O_3. These results showed that the support is not directly involved in the water oxidation reaction and its main purpose is to separate and immobilize the Co_3O_4 nanoclusters.

4.2 Preliminary Work of Carbon Dioxide Reduction Catalysts

4.2.1 Introduction

Additional further work that has been started is the development of a catalysts for the reduction of CO_2 to methanol ($CO_2 + 6e^- + 6H^+ \rightarrow CH_3OH + H_2O$), the other half reaction that was described earlier. While both H_2 and CH_3OH are solar fuels, CH_3OH is more useful for several reasons. At standard conditions, CH_3OH is a liquid, and H_2 is a gas. Liquids are safer to transport than gases, primarily because high pressure or cryogenic systems are required to transport gas phase compounds. Furthermore, the energy density of CH_3OH is a few orders of magnitude higher than that of H_2 (15.6 MJ/L versus 0.01 MJ/L), which means that the storage of CH_3OH is much more efficient with respect to volume. CH_3OH can be blended with gasoline and integrated into existing gasoline infrastructure with minimal modifications; by contrast, the building of a new infrastructure for H_2 would be very expensive. Finally,

CO_2 is utilized as a reactant in the generation of CH_3OH when photocatalysts are used; this is exciting because the generation of a renewable fuel in the simultaneous consumption of a harmful greenhouse gas.

The material chosen for this catalyst is copper oxide: it is cheap, abundant, and its oxides are active under visible light[1-3]. It has also been shown that Cu_2O is able to reduce CO_2 to CH_3OH with high selectivity when loaded onto TiO_2[4]. In the alternate photocatalyst system described earlier, the Cu_xO_y catalyst does not need to be loaded onto TiO_2 because the catalyst does not need to act as light sensitizer; the semiconductor particle, which will be developed in future work, will absorb light and generate electron-hole pairs, and the Cu_xO_y catalyst need only act as a site for electron transfer to adsorbed species.

In order to measure the CO_2 reduction catalytic activity without having to depend on H_2O oxidation half reaction for electrons, a similar system to the $Ru^{2+}(bpy)_3$- $S_2O_8^{2-}$ system is used. This system still contains $Ru(bpy)_3^{2+}$, but an election donor is needed instead of an electron acceptor. Triethanolamine (TEOA) is an optimal choice for an electron donor because it has been shown to yield linear reaction rates for CO_2 reduction[5-7]. This means that any changes in activity that are observed will be not be due to contamination for the oxidized TEOA. The overall process in the system is extremely similar to the $Ru^{2+}(bpy)_3$- $S_2O_8^{2-}$ system: $[Ru(bpy)_3]^{2+}$ absorbs visible light and generates electron-hole pairs and then TEOA donates electrons removing any holes generated when $[Ru(bpy)_3]^{2+}$ absorbs light. As a result, $[Ru(bpy)_3]^{2+}$ can act as an electron source to the Cu_xO_y catalyst. As with the $Ru^{2+}(bpy)_3$- $S_2O_8^{2-}$ system, the primary benefits of this system are that the CO_2

reduction catalytic activity can be determined without the need for another reaction and that electron-hole recombination is prevented.

4.2.2 Synthesis of supported Cu_xO_y catalysts

Like the cobalt oxide catalyst, a silica supported Cu_xO_y catalyst was synthesized. Cu was loaded into the pores of SBA-15 through incipient wetness impregnation. Copper chloride ($CuCl_2$) was mixed with SBA-15 in ethanol (EtOH) in order to ensure that the $CuCl_2$ was well-mixed throughout the SBA-15. The amount of $CuCl_2$ was calculated based on the desired ratio of Cu to SBA-15. So far, 1, 4.8, and 10 percent weight-Cu/weight-SBA-15 were synthesized. Each of these weight ratios will be tested in order to determine which has the highest activity. N-hexane (C_6H_{14}) was added in order to force EtOH into the pores of SBA-15. EtOH moves preferentially into the hydrophilic pores of SBA-15 because it is more hydrophilic than n-hexane.

After incipient wetness impregnation, the next step was the conversion of $CuCl_2$ into CuO and CuO_2. Cu/SBA-15 was exposed to ammonium hydroxide (NH_4OH) vapor in order to form a copper ammonia complex. The complex was calcinated at 400°C in air for three hours to form CuO and CuO_2. The final step was to reduce the catalyst under the flow of H_2 in order to form Cu_xO_y particles. This reduction process converted the CuO and CuO_2—which are inactive for CO_2 reduction—into Cu_2O, which is active for CO_2 reduction. The temperatures chosen for the reduction process ranged from 125°C to 250°C.

4.2.3 Structural Characterization

Transmission electron microscope (TEM) images were recorded on a field emission transmission electron microscope JEM-2010F FasTEM. Powder X-ray diffraction (PXRD) results were collected on a Philips X'pert diffractometer using a Cu Kα source with a scan of 2 s/step and a step size of 0.02^{o} 2θ.

4.2.4 Results and Discussion

XRD patterns can be seen in Figures 4.1 below. In the low angle scans (Figure 4.1a), the (100), (110), and (200) peaks[8] of the *p6mm* hexagonal structure can be seen before and after the impregnation of copper and the reduction under the flow of H_2. This demonstrates that the mesoporous structure of SBA-15 was maintained throughout the catalyst preparation procedure. The slight shift in peak position is likely due to the impregnation of copper.

The broad peak at 22° that is present in all of the Cu/SBA-15 catalyst patterns indicates the presence of amorphous silica. The PXRD data shows that, before reduction under the flow of H_2, CuO and $CuCl_2$ phases are present in the Cu_xO_y/SBA-15 catalyst (Figure 4.1b). The broad nature of the peaks for these phases indicates small particle size. After reduction under the flow of H_2, new peaks form.

At the reduction temperatures of 250°C and 150°C, only Cu and Cu_2O phases can be seen (Figure 4.1c). The peaks at these reduction temperatures were also broad, indicating that small particle size was maintained. At the reduction temperature of 125°C (Figure 4.1d), the $CuCl_2$ phase, is still seen which means that not all of the Cu was reduced while under the flow of H_2 The PXRD patterns show that, at reduction temperatures of 150°C and higher, the desired catalyst is formed. At a reduction temperature of 125°C, the Cu precursor $CuCl_2$ is still present.

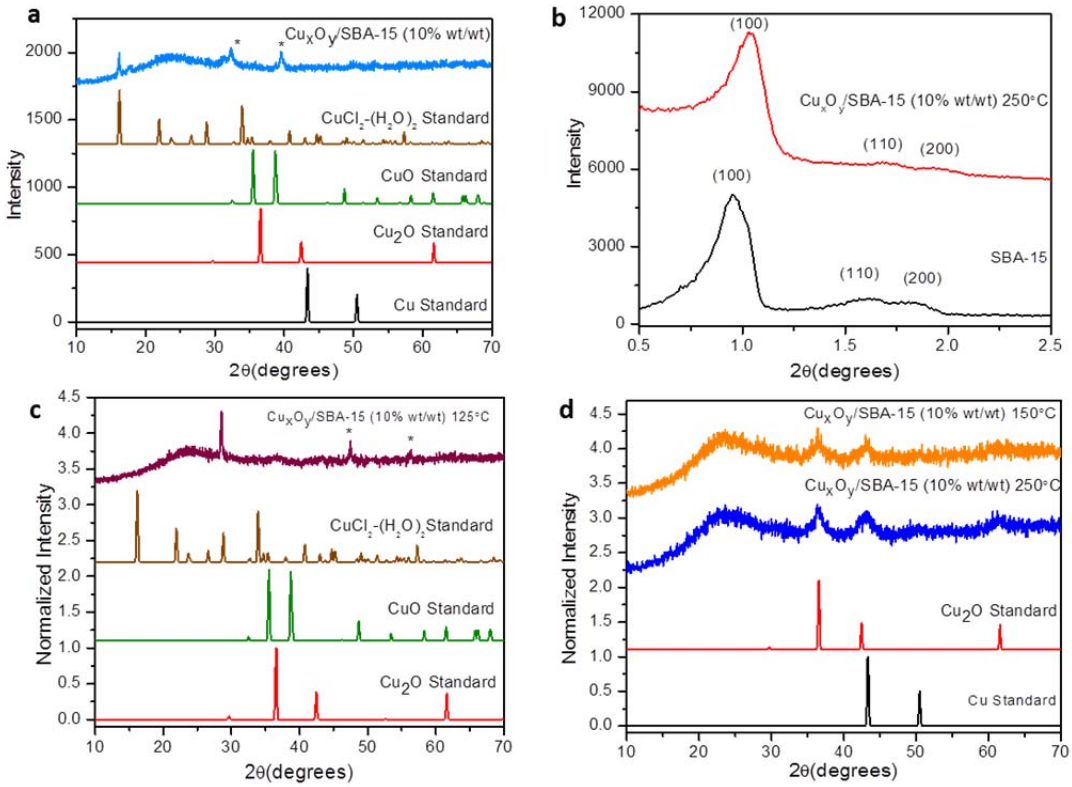

Figure 4.1: PXRD patterns for Cu_xO_y/SBA-15 (10%wt/wt) catalysts. (a) 10%wt/wt catalyst before H_2 reduction, (b) low angle plot of 10% wt/wt catalyst after H_2 reduction at 250°C, (c) wide angle plot of 10% wt/wt catalyst after H_2 reduction at 125°C, (d) wide angle plot of 10% wt/wt catalyst after H_2 reduction at 250°C and 150°C

The TEM images in Figure 4.2 show the ordered structure of SBA-15 and the Cu_xO_y particles. The darker particles on the TEM images are the Cu_xO_y particles. The ordered structure of SBA-15 is visible at all weight % ratios. The average pore size of SBA-15 in all three images is about 10 nm. As the weight ratio of Cu/SBA-15 increases, the number of Cu_xO_y particles increases, but the shape of the Cu_xO_y particles does not change. It can be seen that there are Cu_xO_y particles formed within the mesoporous structure of SBA-15 for all weight ratios. This observation is

confirmed through the Scherrer equation, which can be used to estimate the size of nano-scale particles from the width of XRD peaks. For the 10%wt/wt catalyst reduced at 250°C, the Scherrer equation estimates a size of 8 nm. This is less than the average pore size of the SBA-15, which means that, even at the highest weight ratio, the Cu_xO_y particles are likely in the pores of SBA-15.

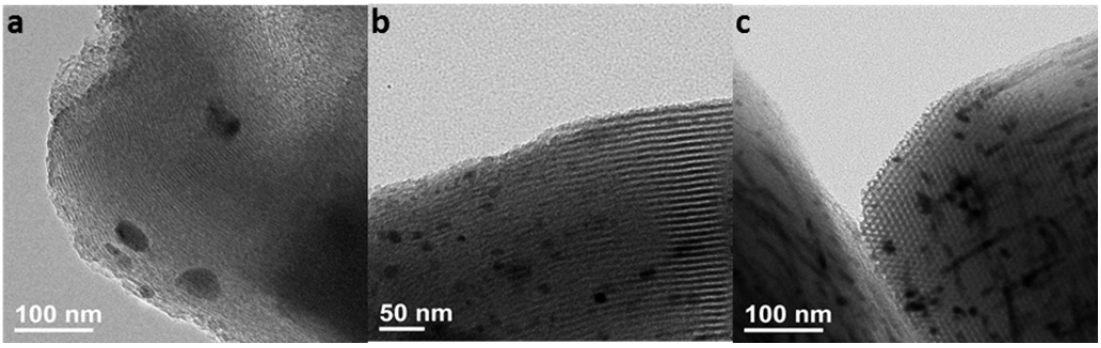

Figure 4.2: TEM images of Cu_xO_y/SBA-15 catalyst reduced at 250°C: (a) 1.0% wt/wt, (b) 4.8% wt/wt, and (c) 10% wt/wt

In order to measure the CO_2 reduction catalytic activity of the Cu_xO_y/SBA-15 catalyst, an in-situ Fourier Transfer Infrared Spectroscopy (FTIR) system was built. When molecules absorb infrared (IR) radiation, they experience changes in vibrational states. These changes in vibrational states cause a bending or stretching of a particular bond, and the frequency of the absorbed IR radiation can be used to identify which bonds are present in a compound. FTIR is a technique that can be used to obtain these absorption spectrums, which lend insight into the reaction mechanism of CO_2 reduction on the Cu_xO_y/SBA-15 catalyst. Due to the in-situ nature of the FTIR system,

it will be possible to detect the formation of new bonds or the breaking of existing bonds in the photoreactor over time without having to disrupt the reaction.

The system for CO_2 reduction consists of the Cu_xO_y /SBA-15 catalyst, TEOA, and $[Ru(bpy)_3]^{2+}$ (as described previously) dispersed in acetonitrile (CH_3CN). Acetonitrile was chosen as the primary solvent because its bonds do not create IR peaks that may interfere with CO_2 reduction analysis. The current setup for the in-situ FTIR system is shown in Figure 4.3. The ALPHA FTIR unit utilizes the diamond Attenuated Total Reflectance (ATR) accessory for measurements. ATR is a sampling technique that allows the liquid from the reactor to be analyzed without any further preparation. The flow-through attachment, which allows for liquid flow from the photoreactor to the ALPHA unit and back again, is on top of the diamond ATR. The glass photoreactor has four outlets: two for the flow of liquid to and from the ALPHA unit and two for the bubbling of gas into the reactor. Precision C-Flex tubing is used to connect the photoreactor to the flow-through attachment, and the Masterflex pump is used to flow liquid from the photoreactor to the ALPHA unit and back. The top of the reactor is sealed with two steel discs and an O-ring. In the center of the steel ring, there is a clear glass disc that allows for the solution inside the reactor to be irradiated with visible light. All of the connections are air-tight, resulting in a closed system.

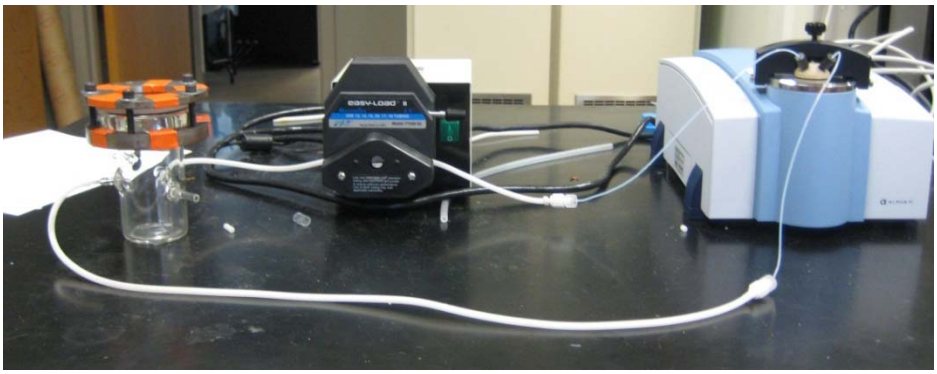

Figure 4.3: In-situ GTIR system with photoreactor (left), Masterflex pump (middle) and Bruker ALPHA FTIR unit with flow through attachment (right)

In order to determine if any new bonds are formed or broken, background spectra of the CO_2 reduction system (acetonitrile, $[Ru(bpy)_3]^{2+}$, TEOA, CO_2) have been taken to determine which peaks are present before any reaction occurs. Some of these background spectra can be seen in Figure 4.4.

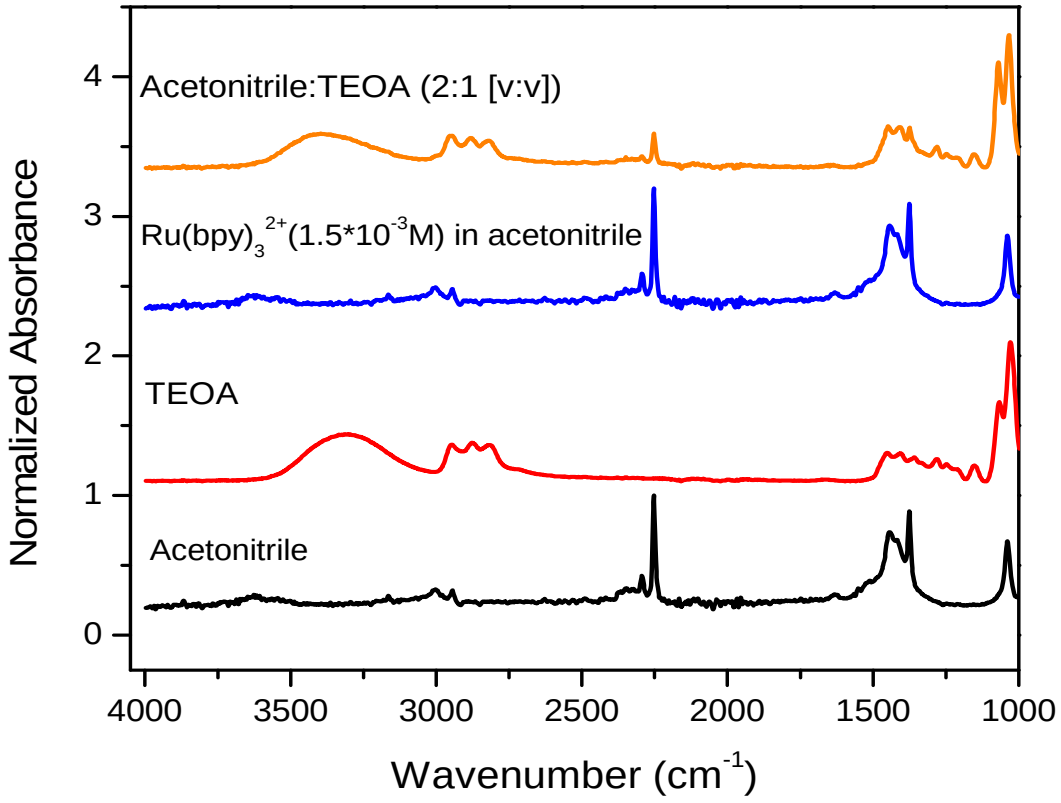

Figure 4.4: Background IR spectra for carbon dioxide reduction system

For acetonitrile, the stretching vibrations can be seen around 2200 cm^{-1} for the C≡N bond, around 3000 cm^{-1} for the CH_3 group. For TEOA, the stretching vibrations can be seen around 3300cm^{-1} for the O-H bond, just before 3000cm^{-1} for CH_2 bonds, and at 1000cm^{-1} for the C-O bond. From these background spectra, it can also be seen when $[Ru(bpy)_3]^{2+}$ is added to acetonitrile at a concentration of $1.5*10^{-3}$M there are no changes in the IR spectrum. When acetonitrile is mixed with TEOA in a 2:1 ratio (v:v), peaks for both compounds are present. With this system it will be difficult to identify methanol, because of the broad O-H peak that is already present from TEOA. However, there are no peaks around 1700cm^{-1}, the region where the peak for the C=O

bond appears. This bond is present in formic acid (HCOOH), another possible product of CO_2 reduction. It will be possible to see if this bond forms during the reaction without interference from other peaks.

4.3 Future Work

The next step for the FTIR system is to test catalytic activity of the Cu_xO_y/SBA-15 catalyst for the CO_2 reduction reaction. By utilizing the background spectra, it will be possible to determine if new bonds form or existing bonds break over the course of the reaction. In particular, the formation of peaks around 1700cm^{-1}, will indicate the formation of C=O bonds which is present in formate, a common side product in this reaction. In order to determine the identity of the formed compounds as well as their concentrations, gas chromatography will be used.

Tetrahydrofuran (THF) and ascorbic acid are also candidates for the CO_2 reduction system, as the primary solvent and electron donor, respectively. These alternate systems will be tested in order to gain insight into the optimal system for CO_2 reduction with the Cu_xO_y/SBA-15 catalyst. In order to obtain different morphologies of Cu_xO_y particles, KIT-6, The new catalyst, Cu_xO_y/KIT-6, would be tested in the same environments as the Cu_xO_y/SBA-15 catalyst in order to determine if it is more or less active than the Cu_xO_y/SBA-15 catalyst. Finally, the “double solvent” technique, previously described in the supported Co_3O_4 work can be used to see if the dispersion of Cu_xO_y particles can be optimized.

4.4 References

(1) Bessekhouad, Y.; Robert, D.; Weber, J. V. Catalysis Today 2005, 101, 315.

(2) Kakuta, S.; Abe, T. Acs Applied Materials & Interfaces 2009, 1, 2707.

(3) Hu, C. C.; Nian, J. N.; Teng, H. Solar Energy Materials and Solar Cells 2008, 92, 1071.

(4) Tseng, I. H.; Wu, J. C. S.; Chou, H. Y. Journal of Catalysis 2004, 221, 432.

(5) Ziessel, R.; Hawecker, J.; Lehn, J. M. Helvetica Chimica Acta 1986, 69, 1065.

(6) Keene, F. R.; Creutz, C.; Sutin, N. Coordination Chemistry Reviews 1985, 64, 247.

(7) Kimura, E.; Wada, S.; Shionoya, M.; Okazaki, Y. Inorganic Chemistry 1994, 33, 770.

(8) Zhao, D. Y.; Feng, J. L.; Huo, Q. S.; Melosh, N.; Fredrickson, G. H.; Chmelka, B. F.; Stucky, G. D. Science 1998, 279, 548.